

# Chemical Abundances in Twelve Red Giants of the Large Magellanic Cloud from High-Resolution Infrared Spectroscopy<sup>1</sup>

Verne V. Smith<sup>2</sup>

Department of Physics, University of Texas El Paso, El Paso, TX 79968 USA;  
verne@barium.physics.utep.edu

Kenneth H. Hinkle

National Optical Astronomy Observatory<sup>3</sup>, P.O. Box 26732, Tucson, AZ 85726 USA;  
khinkle@noao.edu

Katia Cunha<sup>2</sup>

Observatorio Nacional, Rio de Janeiro, Brazil; kcunha@on.br

Bertrand Plez

GRAAL, Universite Montpellier II, Montpellier, France; plez@graal.univ-montp2.fr

David L. Lambert

Department of Astronomy, University of Texas, Austin, TX 78712 USA; dll@anchor.as.utexas.edu

Catherine A. Pilachowski

Astronomy Department, Swain West 319, 727 E. 3<sup>rd</sup> St., Indiana University, Bloomington, IN  
47405 USA; catyp@astro.indiana.edu

Beatriz Barbuy

Universidade de Sao Paulo, IAG, Av. do Matao 1226, Sao Paulo 05508-900, Brazil;  
barbuy@astro.iag.usp.br

Jorge Meléndez

Universidad Nacional Mayor de San Marcos, SPACE & IMCA, Lima, Peru; jorge@astro.iag.usp.br

Suchitra Balachandran

Department of Astronomy, University of Maryland, College Park, MD 20742 USA;  
suchitra@astro.umd.edu

---

<sup>1</sup>Based on observations obtained at the Gemini Observatory, which is operated by the Association of Universities for Research in Astronomy, Inc., under a cooperative agreement with the NSF on behalf of the Gemini partnership: the National Science Foundation (United States), the Particle Physics and Astronomy Research Council (United Kingdom), the National Research Council (Canada), CONICYT (Chile), the Australian Research Council (Australia), CNPq (Brazil), and CONICET (Argentina).

<sup>2</sup>Visiting Astronomer, Gemini South Observatory

<sup>3</sup>Operated by Association of Universities for Research in Astronomy, Inc., under cooperative agreement with the National Science Foundation

Michael S. Bessell

Mount Stromlo & Siding Spring Observatories, Institute of Advanced Studies, The Australian National University, Weston Creek P.O., ACT 2611, Australia; bessell@mso.anu.edu.au

Douglas P. Geisler

Departamento de Fisica, Universidad de Concepcion, Casilla 160 C, Concepcion, Chile;  
doug@kukita.cfm.udec.cl

James E. Hesser

Dominion Astrophysical Observatory, Herzberg Institute of Astrophysics, National Research Council of Canada, 5071 West Sannich Rd., Victoria, BC V9E 2E7, Canada; jim.hesser@nrc.ca

Cláudia Winge

Gemini Observatory, Casilla 603, La Serena, Chile; cwinge@gemini.edu

## ABSTRACT

High-resolution infrared spectra ( $\lambda/\Delta\lambda = 50,000$ ) have been obtained for twelve red-giant members of the Large Magellanic Cloud (LMC) with the Gemini South 8.3m telescope plus Phoenix spectrometer. Two wavelength regions, at 15540Å and 23400Å, were observed. Quantitative chemical abundances of carbon (both  $^{12}\text{C}$  and  $^{13}\text{C}$ ), nitrogen, and oxygen were derived from molecular lines of CO, CN, and OH, while sodium, scandium, titanium, and iron abundances were obtained from neutral atomic lines. The twelve LMC red giants span a metallicity range from  $[\text{Fe}/\text{H}] = -1.1$  to  $-0.3$ . It is found that values for both  $[\text{Na}/\text{Fe}]$  and  $[\text{Ti}/\text{Fe}]$  in the LMC giants fall below their corresponding Galactic values (at these same  $[\text{Fe}/\text{H}]$  abundances) by about  $\sim 0.1$  to  $0.5$  dex; this effect is similar to abundance patterns found in the few dwarf spheroidal galaxies with published abundances. The program red giants all show evidence of first dredge-up mixing of material exposed to the CN-cycle, i.e. low  $^{12}\text{C}/^{13}\text{C}$  ratios, and lower  $^{12}\text{C}$ - with higher  $^{14}\text{N}$ -abundances. The carbon and nitrogen trends are similar to what is observed in samples of Galactic red giants, although the LMC red giants seem to show smaller  $^{12}\text{C}/^{13}\text{C}$  ratios for a given stellar mass. This relatively small difference in the carbon isotope ratios between LMC and Galactic red giants could be due to increased extra mixing in stars of lower metallicity, as suggested previously in the literature. Comparisons of the oxygen to iron ratios in the LMC and the Galaxy indicate that the trend of  $[\text{O}/\text{Fe}]$  versus  $[\text{Fe}/\text{H}]$  in the LMC falls about 0.2 dex below the Galactic trend. Such an offset can be modeled as due to an overall lower rate of supernovae per unit mass in the LMC relative to the Galaxy, as well as a slightly lower ratio of supernovae of type II to supernovae of type Ia.

*Subject headings:* galaxies: abundances — galaxies: individual (Large Magellanic Cloud) — stars: abundances;

## 1. Introduction

The Large Magellanic Cloud (LMC), one of the nearest galaxies and a much smaller system than the Milky Way, is a prime target in which to probe chemical evolution in stellar populations. Unlike the Milky Way, where large fractions of the volume are obscured by dust, the sightlines into most of the LMC are relatively clear, rendering entire populations of stars visible. The LMC's distance demands that detailed stellar abundance studies be based on spectra from 4-8 meter class telescopes and be restricted to rather luminous stars.

Pioneering abundance studies have been conducted on LMC stellar samples already. One basic measure of overall chemical evolution in a stellar system is an age-metallicity relation. In the LMC, Olszewski et al. (1991) and Dopita (1996) provide extensive results, with the Olszewski et al. work based on clusters and Dopita's results derived from planetary nebulae. More recently, Geisler et al. (1997) and Bica et al. (1998) have provided additional results from clusters. In summary, the LMC age-metallicity relation appears to reflect a rapid enrichment phase more than 10 Gyr ago, followed by apparent chemical quiescence until about 2 Gyr ago, when another enrichment period (still ongoing) began.

Additional insights into chemical evolution can be provided by studying elements arising from different nucleosynthetic origins, e.g. Type II supernovae (SN II), Type Ia supernovae (SN Ia), or asymptotic giant branch (AGB) stars. Studies of this type require high-resolution spectra and are still a challenging endeavor to undertake in the LMC. Published abundance distributions for the LMC include Russell & Dopita (1992), Barbuy, Pacheco, & Castro (1994), Hill, Andrievsky, & Spite (1995), Luck et al. (1998), Korn et al. (2000), Hill et al. (2000), Spite et al. (2001), and Korn et al. (2002). The analysed stars include main sequence and supergiant B-stars, supergiant K- to F-stars, and Cepheid variables. For the younger stars ( $\leq 10^8$  yr), these papers find a typical iron abundance of  $[\text{Fe}/\text{H}] \sim -0.3$  for LMC field stars. The oxygen-to-iron abundance ratio in the LMC may be measurably lower than this same ratio at the same  $[\text{Fe}/\text{H}]$  abundance in the Galaxy. The trend of  $[\text{O}/\text{Fe}]$  as a function of  $[\text{Fe}/\text{H}]$  can be a crucial relation in establishing star formation histories in a stellar population. Oxygen is made preferentially in the most massive stars, while iron comes from both massive, core-collapse supernovae (SN II) and the (presumably) binary Type Ia supernovae. The run of the  $\text{O}/\text{Fe}$  ratio with  $\text{Fe}/\text{H}$  in a stellar system is, therefore, a measure of the history of SN II to SN Ia rates, and, hence, the star formation history of the LMC. Carbon and nitrogen abundances may also be lower when compared to Galactic stars at the same  $[\text{Fe}/\text{H}]$ . As C, N, and O (with Ne) are the most abundant heavy elements, their abundances carry much weight in setting the overall metallicity, Z, in a galaxy.

Most of the previous abundance determinations of C, N and O in the LMC have rested on atomic lines, some of which are quite weak, or hampered possibly by non-LTE processes. Because of the importance of the  $\text{O}/\text{Fe}$  ratio to the disentangling of the LMC's star formation history, this study set out to measure oxygen, as well as carbon and nitrogen abundances, in a sample of LMC red giants by observing molecular unblended lines of OH, CO, and CN from

high-resolution infrared (IR) spectra. Using the 8.3m Gemini South reflector, along with the Phoenix high-resolution IR spectrometer, abundances of the isotopes  $^{12}\text{C}$ ,  $^{13}\text{C}$ ,  $^{14}\text{N}$ , and  $^{16}\text{O}$  could be determined along with abundances of Fe, Na, Sc, and Ti.

## 2. Observations & Data Reduction

High-resolution infrared (IR) spectra were obtained of target red-giant stars using the 8.3 m Gemini South reflecting telescope and the NOAO Phoenix spectrometer (Hinkle et al. 1998; 2000; 2002). This instrument is a cryogenically cooled echelle spectrograph that uses order separating filters to isolate individual echelle orders. The detector is a 1024x1024 InSb Aladdin II array. The size of the detector in the dispersion direction limits the wavelength coverage in a single exposure to about  $1550 \text{ km s}^{-1}$ , or  $\sim 120\text{\AA}$  at  $2.3 \mu\text{m}$  and  $\sim 80 \text{ \AA}$  at  $1.6 \mu\text{m}$ . One edge of the detector is blemished so the wavelength coverage on all but the brightest sources is typically trimmed a few percent to avoid this area. The InSb material limits the range of sensitivity to the  $1\text{-}5\mu\text{m}$  wavelength region. However, the thermal brilliance of the sky requires that the observation of fainter sources, e.g. LMC giants, be limited to the non-thermal  $1\text{-}2.4\mu\text{m}$  region. The spectra discussed here were observed with the widest (0.35 arcsecond) slit resulting in a spectral resolution of  $R=\lambda/\Delta\lambda= 50,000$ .

The program star positions, K-magnitudes, and (J-K) colors are listed in Table 1. The positions are taken from the 2-Micron All-Sky Survey (2MASS) database (<http://irsa.ipac.caltech.edu>). The first seven stars listed in Table 1 were selected based upon a color-magnitude diagram constructed using the 2MASS database for two  $15'$  fields in the LMC. The LMC red giant branch is clearly visible in a K versus (J-K) diagram and all program field giants were found to be LMC members based on their radial velocities. The identifying names given to the field stars here were assigned by us as either field 1 or field 2, followed by the star number from our list for that field, i.e. 2.4525 is from field 2 and is number 4525 from that list. In addition to the field stars selected from the 2MASS survey, one star is a bright field supergiant (HV 2568), while four stars in Table 1 were taken from Aaronson & Mould's (1985) IR photometric study of LMC clusters. NGC1898 AM5 is found not to be a member of the cluster (as will be seen from our radial velocity and abundance analysis), but a foreground or background LMC giant.

Each program star was observed along the slit at two, three, or four separate positions separated by  $5''$  on the sky: the delivered image FWHM at the spectrograph varied from  $0.25''\text{-}0.80''$  during the nights that spectra were taken, so stellar images at different positions on the slit were well separated on the detector. Equal integration times were used for a particular program star during a particular set of observations. With this observing strategy, sky and dark backgrounds are removed by subtracting one integration from another (the star being at different positions on the detector array). During each night, 10 flat-field and 10 dark images were recorded for each given wavelength setting of the echelle grating. A hot star, with no intrinsic spectral lines in the regions observed, was also observed each night in each observed wavelength region.

If telluric lines were present in the spectral interval, the hot star was observed at airmasses bracketing the program stars and suitable combinations of the hot star spectra were used to divide out the telluric lines from program star spectra. If no telluric lines fell in the observed region, the hot star was observed only once as a monitor of fringing and general test of data reduction quality. All program stars were observed at two echelle tilts through two different filters: one filter was K4308, with wavelength coverage from 23345 to 23455Å, and the other was H6420, with wavelength coverage from 15505 to 15575Å. Table 2 provides an observational log, showing the number and integration time for each observation, as well as the approximate signal-to-noise (S/N) of each final, reduced spectrum (with reduction as described below).

The array image frames were reduced to one-dimensional, wavelength calibrated spectra with the IRAF<sup>4</sup> set of routines. For a given night and wavelength setting, dark and flat-field frames were averaged and the dark frame was subtracted from the flat-field. The average, dark-subtracted flat-field was normalized and the pairs of differenced program star frames were divided by the normalized flat-field. The aperture containing the stellar signal was defined and traced for each star frame, followed by extraction of the spectrum. For the 23400Å spectra, wavelength calibrations were computed by using a set of telluric wavelengths obtained from the hot star spectra. In the 15540Å region, where there are no telluric lines, wavelengths were set using photospheric lines from the red giants themselves, so no radial-velocity information can be extracted from the spectra observed in this region. The wavelength calibration fits yielded residuals of typically 0.01–0.02Å.

Sample reduced spectra are shown in Figure 1 for both spectral regions in one of the field red giants (2.3256). The top panel shows the 15540Å region and the bottom panel the 23400Å region. The 23400Å region contains a number of telluric absorption lines and this spectrum has been ratioed with the hot star HIP27603 in order to remove telluric absorption lines. The effective airmass of the telluric standard star is adjusted by differently weighted averages of the different integrations on this star until the telluric absorption cancels out as well as possible from the program star. In practice virtually no evidence of such absorption is visible in the program star spectra. In both regions, a number of the spectral lines or features used in the abundance analysis are identified. This figure illustrates both the quality of the spectra and the variety of lines available for study.

### 3. Analysis

The analysis uses a combination of photometry and spectroscopy to determine fundamental stellar parameters (effective temperature, surface gravity, microturbulent velocity, and overall stellar metallicity) and detailed chemical compositions. The high-resolution spectra are analyzed

---

<sup>4</sup>The IRAF software is distributed by the National Optical Astronomy Observatories under contract with the National Science Foundation.

using plane-parallel, LTE model atmospheres that are generated using two different versions of the MARCS code: an older version based largely upon the program as described in Gustaffson et al. (1975), and a more recent version, OSMARCS (Plez, Brett, & Nordlund 1992; Edvardsson et al. 1993; Asplund et al. 1997), which contains more extensive molecular opacities. Abundances derived from both types of models are compared to give some indication of potential model atmosphere systematic effects. The model atmospheres are coupled to the most recent version of the LTE spectrum synthesis code MOOG (Sneden 1973) in order to derive abundances.

### 3.1. Stellar Effective Temperatures

The effective temperatures of the stars are chosen using broadband color (J-K)- $T_{\text{eff}}$  calibrations. Table 1 listed the stars observed along with their K-magnitudes and (J-K) colors. The 2MASS database is the source of the magnitudes and colors for the field giants, while Aaronson & Mould (1985) were used for the cluster members. The 2MASS magnitudes and colors have been transformed to the system defined by Bessell and Brett (1988), as we use  $T_{\text{eff}}$ -calibrations from Bessell, Castelli, & Plez (1998), who use the color system defined in Bessell & Brett (1988). The 2MASS corrections are those defined by Carpenter (2001) in his Appendix A and are fairly small: a constant 0.04 magnitude offset in K, and a small color term that is about 0.03 magnitude in (J-K). Table 3 lists the absolute bolometric magnitudes based upon a distance modulus of 18.5 and K-band bolometric corrections from Bessell et al. (1998): no corrections for reddening in the IR were included here.

Bessell et al. (1998) show that  $T_{\text{eff}}$ -(J-K) relations have a small metallicity dependence and we use their calibration for  $[\text{Fe}/\text{H}] = -0.50$ , which is what is expected for the typical LMC field (Cole, Smecker-Hane, & Gallagher 2000): Table 3 lists these effective temperatures. Other color effective temperature relations are available in the literature. We compare one other source (McWilliam 1990) to the calibrations used here. The mean difference between the effective temperatures from the Bessell et al. (1998) calibration minus those from the McWilliam (1990) calibration is  $+90 \pm 51$  K, suggesting that the temperature scales agree at a level of about 100 K.

### 3.2. Surface Gravities, Microturbulent Velocities, & Iron Abundances

The stellar surface gravity can usually be derived from either ionization equilibria (where, for example, Fe I and Fe II lines are forced to yield the same abundance) or from estimates of stellar luminosity and mass. No ionized atomic lines are detectable in the relatively small IR spectral windows observed here, so gravities are defined by luminosity and mass estimates from the standard relation

$$(g/g_{\odot}) = (M/M_{\odot}) \times (T_{\text{eff}}/T_{\text{eff}}(\odot))^4 \times (L_{\odot}/L).$$

For LMC red giants, bolometric magnitudes (Table 3) and, hence, absolute luminosities are known with some accuracy; the distance modulus adopted is  $18.5 \pm 0.2$ . Mass estimates are obtained using evolutionary tracks. Figure 2 shows plots of  $M_{\text{bol}}$  versus  $T_{\text{eff}}$  for the LMC red giants from this work and model tracks from Schaerer et al. (1993), with the model tracks computed for the metallicity expected for most of LMC program stars ( $[\text{Fe}/\text{H}] = -0.35$ ). Models are shown for  $1.0, 2.0, 3.0, 4.0, 5.0, 7.0$ , and  $10.0 M_{\odot}$  and these tracks stop at the tip of the first ascent of the red giant branch (RGB). Karakas & Lattanzio (2002, private communication) kindly provided tracks for  $1.0, 1.9, 3.0$ , and  $4.0 M_{\odot}$  models that included evolution along the asymptotic giant branch (AGB) and into the thermally pulsing (TP-AGB) phase of evolution (with these models also computed for an LMC metallicity). The two separate sets of models from Schaerer et al. (1993) and Karakas & Lattanzio (2002) agree well from evolution on the ZAMS and onto the RGB; on the AGB and TP-AGB, the tracks become rather complicated and these tracks are not plotted in Figure 2 for the sake of clarity.

The top panel of Figure 2 provides a broad view of stellar evolution and includes the positions of a few other samples of LMC stars from previously published abundance studies, whose results will be compared to those derived here. The Korn et al. (2002) paper is an analysis of 4 main-sequence B-star members of the young cluster NGC2004, while Korn et al. (2000) studied 5 somewhat evolved B-star members in two clusters (NGC2004 again and NGC1818). Hill et al. (1995) derived abundances in 9 field nonvariable (or very slightly variable) F-supergiants. What Figure 2 makes clear is that compared to these earlier LMC studies, the stars sampled here are of rather lower mass. The earlier abundances mentioned above are derived from LMC stars with masses of  $\sim 10 M_{\odot}$ , while the red giants analyzed here have masses closer to  $\sim 2-4 M_{\odot}$ . The mass and evolutionary regimes are quite different and thus our study can add complementary abundance information to what has been derived already for the LMC.

The bottom panel of Figure 2 shows, in more detail, the exact location of the target stars from this study. Except for the massive supergiant, HV2586, the red giants fall in a narrow region crossed by either first ascent giants, or early AGB stars with masses in the range of  $\sim 2-4 M_{\odot}$ . Individual masses were estimated for each LMC red giant and these approximate masses are listed in Table 3: these masses were obtained by comparisons to both the Schaerer et al. (1993) and Karakas & Lattanzio (2002) tracks. The star NGC1898 AM6 is worth a special note as it will turn out to be significantly more metal-poor than the other stars in this sample (with  $[\text{Fe}/\text{H}] = -1.13$ ). Model tracks with  $[\text{Fe}/\text{H}] = -0.35$ , at a given mass, are too red for this giant and more appropriate tracks indicate that it is a lower-mass giant with  $M \sim 1.0 M_{\odot}$ . The surface gravities used for the abundance analysis were then calculated from the mass estimates and are listed in Table 3, rounded to the nearest solar mass. Since no program star, except the obviously massive supergiant HV2586, appears likely to be above  $4 M_{\odot}$ , and none apparently at masses lower than  $2 M_{\odot}$  (except for the metal-poor cluster member NGC1898 AM6), it is likely that errors in the surface gravity do not exceed  $\sim 0.2$  dex, which would not cause a significant error (i.e.,  $\geq 0.15 - 0.20$  dex) in derived abundances.

Modeling the behavior of spectral lines with one-dimensional model atmospheres requires the definition of the microturbulent velocity,  $\xi$ . The value of  $\xi$  is set by the condition that lines of differing line-strengths from the same species result in the same abundances. In the IR spectral windows observed here, the numerous  $^{12}\text{C}^{16}\text{O}$ , hereafter  $^{12}\text{CO}$  lines in the 23400Å window can be used, as the various rotational lines from the (3-1) vibration series exhibit a variety of line-strengths (see Figure 1). The detailed selection of the  $^{12}\text{CO}$  lines is discussed in Section 3.4, but Figure 3 shows an example of the determination of the microturbulent velocity for the cluster-member red giant NGC2203 AM1. The left panels show values of slopes versus  $\xi$  for the abundance versus reduced equivalent-widths (top panel) and abundance versus excitation potential slopes (bottom panel). Both plots show a zero slope at nearly the same value of the microturbulence, indicating that the  $T_{\text{eff}}$  used for this star is a reasonably good value, as the abundance versus excitation potential is sensitive to the temperature, thus, a unique value of  $\xi$  provides a simultaneous fit to both line-strength and excitation potential. The right panels illustrate the quality of the spectral-line data by showing the derived abundances versus both reduced equivalent-width (top panel) and versus excitation potential (bottom panel) for the best-fit value of  $\xi = 3.3 \text{ km s}^{-1}$ . Both trends show effectively zero slopes and small scatter ( $\pm 0.05$  dex in the  $^{12}\text{C}$  abundance). The derived microturbulent velocities are listed in Table 3.

The right panels in Figure 3 also illustrate an experiment conducted on line formation in the model atmospheres. The  $^{12}\text{CO}$  lines are formed over a range of optical depths in the atmosphere, with strong lines being formed preferentially higher compared to weaker lines. The filled circles in these panels show results for a “standard” model atmosphere used in the abundance analysis: standard here means the atmosphere extends to optical depths, defined at  $\lambda=5000\text{\AA}$  as low as  $\tau_{5000} = 10^{-4}$ , at which point the atmosphere is truncated. The open squares show abundances from the  $^{12}\text{CO}$  lines for a model that has been truncated at  $\tau_{5000} = 10^{-3}$ : as some of the  $^{12}\text{CO}$  lines are the strongest lines in the spectra, if substantial contributions to their absorption were occurring near  $\tau_{5000} \sim 10^{-4}$ , truncating the models here would result in incorrect abundances. Clearly, truncating at either  $10^{-3}$  or  $10^{-4}$  in optical depth has no significant effect ( $\leq 0.01$ -0.02 dex) on derived abundances, and the optical depth structures of the models are adequate.

Earlier abundance studies of Galactic red giants that overlap somewhat the effective temperatures and gravities of the stars studied here were Smith & Lambert (1985, 1986, 1990) and it is instructive to compare values of the microturbulence derived from those papers and the microturbulent velocities measured here; the Smith & Lambert analyses relied on near-IR Fe I lines as the primary indicators with which to set  $\xi$ , while using the  $^{12}\text{CO}$  lines as secondary checks. The top panel of Figure 4 is a plot of  $\xi$  versus absolute bolometric magnitude for the LMC red giants and the Galactic stars from the Smith & Lambert papers. It appears that the lower luminosity giants have a typical  $\xi = 2.0 \text{ km s}^{-1}$ , but at luminosities greater than  $M_{\text{bol}} \sim -2.5$ , there is a trend of increasing values of  $\xi$  with increasing absolute magnitude, as well as increasing amounts of scatter. The LMC red giants fall right within the scatter as defined by the Galactic giants, with the LMC sample tending to be composed of stars of slightly higher luminosities than

the samples of Galactic stars studied by Smith & Lambert (1985, 1986, 1990), but exhibiting the same basic behavior in terms of the microturbulence. The bottom panel of Figure 4 is in a similar vein to the top panel: here  $\xi$  is plotted versus  $\log g$ . Microturbulent velocities for the Milky Way giants cluster around  $2.0 \text{ km s}^{-1}$  for the higher gravity stars ( $\log g \geq 1.0$ ), but then  $\xi$  increases both in magnitude and scatter as gravity decreases. The overlap between Galactic and LMC giants is essentially perfect.

The metallicity is estimated from the  $15540\text{\AA}$  window where three Fe I lines are measurable as largely unblended features. The next section covers the linelist selections for the various species in detail, but the [Fe/H] values listed in Table 3 are from these three lines, using gf-values set by fits to the IR Arcturus spectra atlas (Hinkle, Wallace, & Livingston 1995) using the Fe abundance determined from optical Fe I and Fe II lines (Smith et al. 2000). The parameters for  $\alpha$  Boo (Arcturus) adopted here are those derived by Smith et al. (2000):  $T_{\text{eff}} = 4300\text{K}$ ,  $\log g = 1.7$ ,  $\xi = 1.6 \text{ km s}^{-1}$ , and [Fe/H] = -0.72.

The last column of Table 3 lists the heliocentric radial velocities of the program stars as determined from the sample of nine  $^{12}\text{CO}$  lines used to set the microturbulence. From the radial velocities it is found that all program stars are LMC members; Prevot et al. (1985) find velocities of field stars in the LMC to range from  $\sim +250$  to  $+310 \text{ km s}^{-1}$ . The two clusters in our sample were also observed by Olszewski et al. (1991) for both radial velocities and metallicities (not the same stars as observed here, however). In the case of NGC2203, Olszewski et al. (1991) find a mean radial velocity of  $+243 \text{ km s}^{-1}$ , which is close to the  $+253 \text{ km s}^{-1}$  found for the two member stars in this sample. They also derive a cluster metallicity of [Fe/H] = -0.53: a value similar to what we find for AM1 (-0.67) and AM2 (-0.61). For NGC1898, Olszewski et al. (1991) observe a mean cluster velocity of  $+210 \text{ km s}^{-1}$  and a metallicity of [Fe/H] = -1.37. This radial velocity and abundance are close to what we find for AM6 ( $V = +219 \text{ km s}^{-1}$  and [Fe/H] = -1.1). For the other star, AM5, we find  $V = +255 \text{ km s}^{-1}$  and [Fe/H] = -0.50: quite different from Olszewski et al. (1991) or what we find for AM6. This star is almost certainly a cluster non-member, however, its velocity indicates that it is a member of the LMC. It is either a foreground or background LMC red giant in the field of NGC1898.

### 3.3. The Atomic Lines Used: Fe I, Na I, Sc I, and Ti I

In the two spectral intervals sampled, a handful of atomic lines are detectable which are largely unblended and single. These lines are listed in Table 4, along with the measured equivalent widths from the twelve program LMC red giants. The excitation energies are from the Kurucz & Bell (1995) lists, while the gf-values have been adjusted to provide the same abundances from these lines in  $\alpha$  Boo (Hinkle et al. 1995) as found from the analysis of this standard star in conjunction with analyses of  $\omega$  Cen red giants (Smith et al. 2000). Table 4 lists the line data and equivalent widths for all 12 of the program stars.

### 3.4. The Molecular Lines Used for the CNO Abundances: CO, OH, and CN

The IR windows were chosen to provide molecular lines from which to derive the C, N, and O abundances. The 23400Å region includes lines of the CO first-overtone vibrationa-rotation bands. The 15540Å region includes lines of the OH first-overtone vibration-rotation bands and the CN Red system. Partial pressures of C and O are coupled through the formation of CO and to a lesser extent of OH and H<sub>2</sub>O. The partial pressure of N is controlled almost exclusively by formation of N<sub>2</sub>. Minor influences of other molecules was taken fully into account. A simultaneous analysis of CO and OH lines provides the C and O elemental abundances. Analysis of the CN lines and the C abundance give the N abundance.

The wavelengths, excitation potentials, and gf-values for the CO vibration-rotation lines are from Goorvitch (1994), with the  $\Delta v=2$  lines in the 23400Å region being used. The <sup>12</sup>CO lines measured span a range in line strength and  $\chi$ , and were used to set the microturbulence as well as provide a check on the adopted  $T_{\text{eff}}$  from the (J-K) photometry. The CO dissociation energy was taken as  $D_0= 11.090\text{eV}$ . In addition to the <sup>12</sup>CO lines, the <sup>13</sup>CO (2-0) bandhead falls at the red edge of the 23400Å setting in all but one program star, and synthesis of this bandhead was used to derive a <sup>13</sup>C abundance (tabulated as a <sup>12</sup>C/<sup>13</sup>C ratio).

The spectral region near 15540Å was selected as it contains a number of relatively isolated and unblended OH lines, as used in previous oxygen analyses by Balachandran & Carney (1996), Melendez, Barbuy, & Spite (2001), and Meléndez & Barbuy (2002). Asplund & Garcia Pérez (2001) have pointed out that strong OH lines may be sensitive to the effects of temperature differences and granulation that are found in the 3D model atmospheres, but not in the 1D models; however their calculations covered effective temperatures that are considerably hotter ( $T_{\text{eff}}= 5800\text{-}6200\text{K}$ ) than those found here. Nissen et al. (2002) point out that the granulation effects on the OH lines from the 3D models are expected to decline with decreasing effective temperature. Meléndez & Barbuy (2002) confirmed that oxygen abundances derived from the stronger lines are higher than for the weaker OH lines, again however, for stars that are distinctly hotter than those sampled here. The differences found by Meléndez & Barbuy (2002) are more pronounced for more metal-poor stars and disappear for stars with  $[\text{Fe}/\text{H}]\geq -1$ . The combination of lower effective temperatures and higher metallicities in the stars sampled here why this effect is not found in our oxygen abundances. The wavelengths, excitation potentials, and gf-values are from Goldman et al. (1998), with the dissociation energy being  $D_0= 4.392\text{eV}$  (Huber & Herzberg 1979).

Nitrogen abundances are based on five CN lines in the 15540Å spectral region (these CN lines are weaker than the CO and OH lines, but are well-defined and typically unblended). The CN lines were chosen from a linelist extracted from a masterlist compiled by B. Plez as described in Hill et al. (2002). The CN dissociation energy is  $D_0= 7.77\text{ eV}$  (Costes et al. 1990).

The molecular line data, as well as the measured equivalent widths are listed in Table 4.

### 3.5. Errors from Stellar Parameter Uncertainties and Final Abundances

As already discussed in Section 3.1, uncertainties exist in  $T_{\text{eff}}$  of at least  $\sim 100$ K and gravities may be uncertain by about  $\pm 0.2$  dex. Fits to the  $^{12}\text{CO}$  lines to determine  $\xi$  constrain this parameter to  $\pm 0.2$  to  $0.3$   $\text{km s}^{-1}$ . In order to investigate how these parameter uncertainties manifest themselves into abundance changes, the model for the program star 2.4525, which has an effective temperature near the middle of the program star distribution, was perturbed by  $+100$ K in  $T_{\text{eff}}$ ,  $+0.2$  dex in  $\log g$ , and  $+0.2$   $\text{km s}^{-1}$ , respectively, and abundances computed for each perturbation. These abundance changes are listed in Table 5 for each species used in the abundance analysis. These changes can be assumed to be quasi-linear for small changes in the stellar parameters across the range of values found for this sample of red giants and be used to assess the overall uncertainties in the abundance analysis.

Systematic effects are always possible, for example, due to the choice of type of model atmosphere. This possibility was investigated by comparing abundances derived from two different sets of model atmospheres, one from the older MARCS program and the other from the newer OSMARCS code. In none of the stellar parameters spanned by the program stars was it found that derived abundance differences exceeded 0.10 dex. In the deeper layers (where  $\tau_{5000} \geq 0.6$ ) the two sets of models agree in temperature and pressure. In regions where spectral lines form (typically  $\tau_{5000} \sim 0.1$ ), differences are still essentially zero at  $T_{\text{eff}} = 3800$ K, but the OSMARCS models become slightly warmer (by about 40K), and have higher gas pressures (by about 20%) for  $T_{\text{eff}} = 3600$ K. The lines affected most by the differing models at this effective temperature were from OH (note the temperature sensitivity in Table 5), however, the effects were small and of no significant consequence to the abundances reported here.

Final abundances, based upon the OSMARCS models, are listed in Table 6 in the system of  $A(x) = \log \epsilon(x) = \log[n(x)/n(\text{H})] + 12$ . The  $^{13}\text{C}$  abundances are reported in the traditional form of  $^{12}\text{C}$  to  $^{13}\text{C}$  ratios. For species with abundances derived from three or more lines, the standard deviation of the mean is also shown: this provides some rough estimate of the quality of the spectra used in the analysis. All abundances were based ultimately on spectrum synthesis, although the equivalent widths listed in Table 4 were used for a first-cut abundance analysis. Included in Table 6 are the adopted abundances in the Sun for the elements studied, as well as for the well-studied, metal-poor red giant  $\alpha$  Boo. The  $\alpha$  Boo abundances for Fe, Na, Sc, and Ti are those from Smith et al. (2000); the atomic-line gf-values were adjusted so as to yield these abundances in  $\alpha$  Boo from an analysis of these lines in the IR Atlas spectrum of this star (Hinkle et al. 1995). The abundances in  $\alpha$  Boo for C, N, and O (including  $^{13}\text{C}$ ) were derived from the same spectral regions and lines of CO, OH, and CN as used in the analysis of the LMC program stars.

Examples of two spectral syntheses in LMC red giants are shown in Figure 5. The top panel shows one region containing three  $^{12}\text{CO}$  lines (of differing strengths) and a Sc I line. The spectrum displayed is that from LMC 1.6 and three separate  $^{12}\text{C}$  and Sc abundances are illustrated in the syntheses. The comparisons between observed and model spectra are excellent. The bottom panel

shows two of the OH lines in NGC1898 AM6 with, again, three different oxygen abundances in the synthetic spectra. Examples of observed and synthetic spectra of the blended  $^{13}\text{CO}$ (2-0) bandhead are displayed in Figure 6. The top panel shows the LMC field giant 2.1158, which has an estimated mass of  $\sim 3\text{M}_\odot$  (Figure 2 and Table 3). Syntheses with three different isotopic carbon ratios are shown, with  $^{12}\text{C}/^{13}\text{C} = 17$  providing the best fit. The cluster member AM6 of NGC1898 is shown in the bottom panel to illustrate  $^{13}\text{CO}$  in a lower-mass ( $\sim 1\text{M}_\odot$ ), lower-metallicity ( $[\text{Fe}/\text{H}] = -1.1$ ) giant. In this star, a much lower isotopic ratio is derived, with  $^{12}\text{C}/^{13}\text{C} = 3.5$ .

### 3.6. The Abundances

## 4. Discussion

Observational understanding of a stellar system’s chemical evolution must pursue a selection of elements whose stellar surface abundances are considered to reflect faithfully the composition of the gas from which the stars formed. Here, Na, Sc, Ti, and Fe may plausibly be deemed such a selection. Below, we discuss some implications of our abundances, primarily, by contrasting abundance ratios relative to Fe in the LMC, the Galaxy, and other systems.

On the other hand, surface abundances of C and N in red giants are well recognized to be affected by convective mixing as red giants. This mixing rearranges the C and N abundances and obscures the original abundances which betray the chemical evolution of the stellar system. We compare C and N in LMC and Galactic red giants.

Oxygen is likely unaffected by the convective mixing until the giant evolves to the asymptotic giant branch. Here, we assume O is a probe of chemical evolution, and discuss the O/Fe ratio in the LMC and the Galaxy.

### 4.1. The LMC Iron Abundances

The red-giant sample here consists of nine stars that are not associated with any clusters and are thus categorized as field stars, and three stars that are members of clusters (1 in NGC1898 and 2 in NGC2203). Recently, Cole, Smecker-Hane, & Gallagher (2000) have begun to map the field metallicity distribution in the LMC, and present values of  $[\text{Fe}/\text{H}]$  (derived from Ca II IR-triplet measurements) for 38 field red giants. Their distribution for  $[\text{Fe}/\text{H}]$  is shown in the top panel of Figure 7. This metallicity distribution peaks at about  $[\text{Fe}/\text{H}] = -0.5$ , with a fairly sharp cutoff at  $-0.25$ , and a diminishing tail down to  $[\text{Fe}/\text{H}]$  of about  $-1.6$ . Our sample of field stars is small and the resulting  $[\text{Fe}/\text{H}]$  distribution is shown in the bottom panel of Figure 7; clearly the overlap in metallicity between the two samples is perfect. The details of the shape of the metallicity distribution function for the field stars studied here cannot be well-defined with only nine stars, so a detailed comparison with the Cole et al. (2000) results requires a larger sample, but the overall

agreement is encouraging.

The two clusters sampled in this study have both had their metallicities measured by Olszewski et al. (1991), who also used the Ca II IR-triplet method. For NGC1898, they find  $[Fe/H] = -1.37$ , while we find  $[Fe/H] = -1.13$  for member AM5. With estimated total uncertainties of  $\sim 0.16$  dex in Fe I as derived from this study, plus the uncertainties from the Olszewski et al. (1991) work, a difference of 0.24 dex signifies quite good agreement for this cluster. The other cluster common to both studies is NGC2203, which has an average  $[Fe/H] = -0.64$  from 2 members analyzed here (AM1 and AM2), while Olszewski et al. (1991) find  $[Fe/H] = -0.53$ : again quite good agreement between two very different types of analyses.

#### 4.2. Sodium, Scandium, and Titanium Abundances

Commonly, results of stellar abundance analyses are expressed as the quantity  $[X/Fe]$ . The Na, Sc, and Ti abundances in Table 6 give mean values  $[Na/Fe] = -0.30$ ,  $[Sc/Fe] = 0.0$ , and  $[Ti/Fe] = -0.18$  with a star-to-star scatter most probably dominated by measurement errors. These results compare fairly favorably with measurements from LMC F-G supergiants and Cepheids: for example, Hill et al. (1995) give  $([Na/Fe], [Sc/Fe], [Ti/Fe]) = (-0.2, -0.1, 0.0)$  for  $[Fe/H] \sim -0.3$  supergiants referenced to the Galactic supergiant Canopus, and Luck et al. (1998) give  $(-0.15, -0.14, 0.07)$  for similar Cepheids with respect to Galactic Cepheids. Use of Galactic comparisons minimizes systematic errors. At the same  $[Fe/H]$  as the LMC stars, Galactic stars show slightly positive values of  $[Na/Fe]$  and  $[Ti/Fe]$  but a  $[Sc/Fe]$  close to zero. At the same  $[Fe/H]$  as the LMC stars, Galactic stars show slightly positive values of  $[Na/Fe]$  and  $[Ti/Fe]$  but a  $[Sc/Fe]$  close to zero. The mild Na and Ti underabundances of the LMC stars relative to Galactic stars of the same  $[Fe/H]$  is likely attributable to the same factors responsible for the lower  $[O/Fe]$  (see below). In addition, the underabundances of Na and Ti, relative to Fe, are also found in the few dwarf spheroidal galaxies with published abundances, e.g. Shetrone, Cote, & Sargent (2001).

#### 4.3. Carbon and Nitrogen Abundances

Carbon and nitrogen abundances are altered during mixing in red giants, as material exposed to the CN-cycle is brought to the star's surface. The  $^{12}\text{C}$  abundance decreases, the  $^{14}\text{N}$  abundance increases, and the  $^{12}\text{C}/^{13}\text{C}$  ratio decreases, but the sum of the  $^{12}\text{C}$ ,  $^{13}\text{C}$ , and  $^{14}\text{N}$  is conserved. This mixing in first ascent and early-AGB red giants is not expected to alter the  $^{16}\text{O}$  abundance.

Figure 8 investigates the  $^{12}\text{C}$  and  $^{14}\text{N}$  abundances in the LMC red giants in comparison to other samples of stars, both in the LMC and in the Galaxy. The abundances of  $^{14}\text{N}$  are plotted versus the abundances of  $^{12}\text{C}$ . The solar symbol is located at  $A^{12}\text{C}=8.41$  (Allende Prieto, Lambert, & Asplund 2002—from their 1D MARCS model) and  $A^{14}\text{N}=7.93$  (Holweger 2001) and the dashed line represents equal changes in both carbon-12 and nitrogen-14. The solid curves are various

“mixing curves” in which initial abundances of carbon and nitrogen are changed in such a way that their sum remains constant: as  $^{12}\text{C}$  decreases,  $^{14}\text{N}$  increases to mimic red-giant mixing of material consisting of increasing exposure to the CN-cycle. The open circles show the  $^{12}\text{C}$  and  $^{14}\text{N}$  abundances in Galactic disk M-giants from Smith & Lambert (1985; 1986; 1990) and these giants are well-represented by a CN-cycle mixing curve defined by approximate solar carbon and nitrogen initial abundances. The four-pointed crosses are s-process enriched MS and S stars, also from the Smith & Lambert papers and are plotted as different symbols because the photospheres of these giants have presumably been contaminated by material from the third dredge-up, associated with  $^4\text{He}$ -burning thermal pulses along the AGB. Such stars quite possibly have had primary  $^{12}\text{C}$  added to their surfaces and might be expected to evolve away from a simple CN-cycle mixing curve. What should be noted concerning the MS/S stars, however, are the few examples which show very large  $^{14}\text{N}$  abundances. These objects are AGB stars that have undergone hot-bottom burning (e.g. D’Antona & Mazzitelli 1996), where some amount of primary  $^{12}\text{C}$  produced during thermal pulses on the AGB is converted to  $^{14}\text{N}$ , via the CN-cycle, at the base of a deep convective envelope.

The LMC red giants analyzed here are plotted in Figure 8 as filled circles and fall in a much different region than the Galactic red giants. The two mixing curves that define approximately the region in the carbon-nitrogen plane where the LMC giants fall begin at lower initial carbon and nitrogen abundances. As initial values, we used the recent paper by Korn et al. (2002) that presents abundances for 4 true main-sequence B-star members of the young LMC cluster NGC2004. They conducted a non-LTE abundance analysis and their results for C and N are shown as the open squares in Figure 8. Using initial C and N abundances that bracket the Korn et al. (2002) abundances, the resulting CN-mixing curves provide excellent approximations to the behavior of the field LMC red giants. One of the results for LMC initial abundances, as indicated by Korn et al. (2002), was a lower value for both  $[\text{C}/\text{Fe}]$  and  $[\text{N}/\text{Fe}]$  in the LMC: such mixing lines, beginning at values of  $\sim-0.3$  dex in  $[\text{C}/\text{Fe}]$  and  $[\text{N}/\text{Fe}]$ , go right through the regions defined by the red giant abundances. An additional conclusion from the comparison of the carbon and nitrogen abundances in both the main-sequence B-stars and the red giants, is that simple CN mixing does an excellent job of describing the dredge-up in this sample of red giants; no evidence of deeper mixing, or of hot bottom burning, is found: these processes might lower the star’s  $^{16}\text{O}$  abundance through conversion of some  $^{16}\text{O}$  to  $^{14}\text{N}$  through the ON-cycles.

The constraint on possible oxygen depletions can be strengthened further by investigating the C/N abundance ratios. Most of the LMC giants in Figure 8 fall at values of  $[\text{C}/\text{Fe}]$  that are about 0.6 to 0.8 dex below their probable initial values (as suggested by the Korn et al. 2002 results). At these levels of carbon-12 depletions, for the case of only CN-cycle mixing, the expected C/N ratios would be about 6 or less; all of the measured C/N ratios calculated from the abundances in Table 6 fit this constraint. The C/N ratio will increase over this value if additional nitrogen is added from the conversion of  $^{16}\text{O}$  to  $^{14}\text{N}$  via the ON cycles. Because oxygen is the most abundant member of the CNO trio, even a relatively modest depletion will measurably increase the nitrogen abundance. Given a plausible initial oxygen abundance as determined by Korn et al.

(2002), a decrease in  $^{16}\text{O}$  of 0.2 dex would increase the C/N ratio to values of 8-10 in the regime of carbon depletions observed in the present sample of LMC red giants; such a large ratio is not found in any of the program stars. The LMC red giants studied here appear to have effectively unaltered  $^{16}\text{O}$ .

The  $^{12}\text{C}/^{13}\text{C}$  ratio is another abundance indicator that is sensitive to stellar mixing on the red giant branch. The initial ratio is expected to be quite large ( $\sim 40\text{-}90$ ), while first dredge-up lowers this ratio to  $\sim 18\text{-}26$  for stars in the mass range from  $M \sim 1\text{-}8\text{M}_\odot$  according to standard stellar models (e.g., Charbonnel 1994; but also Iben 1964). It has been known for some time that low-mass field giants exhibited lower  $^{12}\text{C}/^{13}\text{C}$  ratios than predicted by standard models, with Keller, Sneden, & Pilachowski (2002) providing recent results of a discussion of this effect. Masses for giant-star members of clusters can be determined more accurately than masses for field giants, and the effect of lower  $^{12}\text{C}/^{13}\text{C}$  ratios in lower-mass giants has been quantified by Gilroy (1989) using open clusters. Her results of  $^{12}\text{C}/^{13}\text{C}$  versus giant mass are plotted in Figure 9 as the open squares. Above a mass of about  $2.0\text{-}2.5\text{M}_\odot$ , the values of  $^{12}\text{C}/^{13}\text{C}$  are 22-30 and agree reasonably well with standard stellar models of first dredge-up. In the lower-mass giants, however, Gilroy (1989) finds steadily decreasing  $^{12}\text{C}/^{13}\text{C}$  ratios with decreasing mass, in contradiction to standard models. The  $^{12}\text{C}/^{13}\text{C}$  ratios derived here for the LMC red giants are also plotted in Figure 9 as the filled circles. The masses for the LMC giants are estimated to only  $\pm 0.5\text{M}_\odot$  and are based on the model tracks from Figure 2: these masses should be viewed as crude estimates. Nevertheless, there is a general trend of lower  $^{12}\text{C}/^{13}\text{C}$  ratios with lower masses that tracks the Gilroy (1989) trend rather well, although offset to lower isotopic carbon-12 to -13 ratios for a given mass. Charbonnel (1994) and Charbonnel, Brown, & Wallerstein (1998) investigate the lower  $^{12}\text{C}/^{13}\text{C}$  values in the lower-mass red giants and suggest that extra-mixing, possibly driven by meridional circulation and rotationally induced turbulence can explain the lower  $^{12}\text{C}/^{13}\text{C}$  ratios. In their model, extra-mixing is inhibited by mean molecular weight gradients, which increase with increasing metallicity, so they predict more extensive mixing (and lower  $^{12}\text{C}/^{13}\text{C}$  ratios for a given-mass giant) at lower metallicities. The offset between Gilroy's (1989) trend and the LMC trend may be due to this metallicity effect.

The  $^{12}\text{C}/^{13}\text{C}$  ratio of 45 in NGC2203 AM2 deserves some mention. Although the errorbars on this measurement are large, it still falls well above the trend of  $^{12}\text{C}/^{13}\text{C}$  with mass found for the other LMC red giants. One possibility is that this star has begun dredge-up as an AGB star and some  $^{12}\text{C}$  (produced from  $^4\text{He}$ -burning) has been added to the photosphere. If the  $^{12}\text{C}$  abundance were increased by 0.15 dex due to such dredge-up, the observed current  $^{12}\text{C}/^{13}\text{C}$  ratio of 45 would have been 30 before the addition of extra  $^{12}\text{C}$ : within the scatter of the other red giants. Until more LMC red giants are observed, such an explanation of the anomalous position of NGC2203 AM2 in Figure 9 is speculation.

#### 4.4. The Oxygen Abundances

On the assumption that the oxygen abundance is left unaltered by the convective mixing, an assumption supported by the  $^{12}\text{C}$ ,  $^{13}\text{C}$ , and  $^{14}\text{N}$  abundances of the LMC red giants, the O/Fe ratio may be used as a tracer of chemical evolution. The [O/Fe] values run from -0.3 to +0.3 with a hint that they increase with decreasing [Fe/H]. Oxygen to iron abundances from a large number of Galactic and LMC studies, presented as [O/Fe] versus [Fe/H], are brought together in Figure 10: the LMC red-giant results from this study are plotted as filled circles. The Galactic samples of field stars shown in this figure are taken from Edvardsson et al. (1993), shown as open circles, Nissen & Edvardsson (1992) shown as open triangles, Cunha, Smith, & Lambert (1995) shown as open hexagons, and Smith, Cunha, & King (2001) shown as open squares (the Galactic results are plotted as smaller symbols simply to keep these numerous points from falling on top of each other and obliterating their visibility). The open pentagons at low metallicity are the recent results for Galactic stars from Melendez & Barbay (2002) using the IR OH v-r lines: this paper also includes the earlier results from Melendez, Barbay, & Spite (2001). Other low-metallicity results for [O/Fe] are from Barbay (1988) and Nissen et al. (2002), shown as asterisks and three-pointed stars, respectively. Additional [O/Fe] values for the LMC are shown as comparisons to the red giants observed here: the filled triangles are from Korn et al. (2002) for main-sequence B-stars, the filled squares are from Hill et al. (1995) for F-supergiants, and the filled pentagons are from Hill et al. (2000) and Spite et al. (2001) for old clusters and globular clusters. Figure 10 shows that, over the metallicity range of  $[\text{Fe}/\text{H}] \sim -1.0$  to -0.2, the LMC stars fall about 0.2-0.3 dex below stars in the Milky Way. The fact that main-sequence B-stars, F supergiants, and cool, red giants all yield the same results from independent analyses using very different sets of lines (O II and Fe III for B stars, weak O I 6158Å lines and Fe II for F supergiants, and Fe I plus OH for the red giants) suggests strongly that this is now a well established trend.

The common interpretation of the different [O/Fe] - [Fe/H] relations is that star formation in the LMC occurred in an early burst. Interruption of star formation reduced the input of oxygen into the interstellar gas. In this interval, SN Ia delivered iron and so brought the O/Fe down. In the Galaxy, star formation was less affected by bursts, and O/Fe remained at its “high” value to a higher [Fe/H] than in the LMC. The solid curves shown in Figure 10 are a simple interpretation of the differing values of [O/Fe] in the Milky Way versus the LMC. These curves were generated by taking yields from supernovae of types II and Ia and adding the processed elements into a unit mass of gas over time. The rate at which the abundances grow with time depends on the supernovae rate per unit mass of gas. This rate is normalized by assuming a rate of one SN II per 100 years and one SN Ia per 300 years in the Milky Way, with the mass taken to be  $10^{11}\text{M}_\odot$ . Oxygen mass yields for SN II were taken from Arnett (1999) and convolved with a Salpeter mass function to yield an average mass of  $1.5\text{M}_\odot$  ejected per SN II. Iron yields for SN II were similar to that from Timmes, Woosley, & Weaver (1995), and set at  $0.15\text{M}_\odot$  per SN II. With the rates and yields set for the Milky Way SN II, it remained to set both the Fe yield from SN Ia and the time delay for their initial contribution to chemical evolution. In order to fit the Milky Way trend as

shown in Figure 10, it was necessary to set the SN Ia Fe yield to  $0.7M_{\odot}$  per SN Ia and to use a time delay of 1.5 Gyr: both of these values are reasonable in such a simple approximation. The resulting curve does a fairly good job of following the values of [O/Fe] versus [Fe/H] in the Milky Way, with the final point on the calculated curve shown being reached after a time of 12 Gyr. The other curve shown was generated as an approximation to the LMC trend of [O/Fe] versus [Fe/H]. Although not a unique solution, this curve was generated by simply lowering the SN II rate per unit mass in the LMC by a factor of 3 and the SN Ia rate by a factor of 2 (the SN II and Ia O and Fe yields and SN Ia time delay were the same). This very simple numerical model indicates the [O/Fe] abundance ratios in the LMC can be understood as arising from both a slower rate of SN II per unit mass (caused presumably by a lower average star formation rate per unit mass of gas) and a slightly enhanced ratio of SN Ia rates to SN II rates in the LMC. These results are in rough agreement with those suggested by the analytical chemical evolution models of Pagel & Tautvaisiene (1998).

## 5. Conclusions

Abundances of seven elements (C, N, O, Na, Sc, Ti, and Fe) have been measured in twelve red-giant members of the LMC from high-resolution IR spectra obtained with Gemini South plus Phoenix. Using IR spectra it is possible to extract quantitative chemical abundances for a number of elements in somewhat lower-mass stars ( $M \sim 2-4M_{\odot}$  red giants) in the LMC than previous high-resolution optical spectroscopic studies of main-sequence B-stars or F to K supergiants (with  $M \sim 8-10M_{\odot}$ ). The IR abundance analyses add complementary stellar mass targets to the earlier works. In addition, the molecular lines of such species as CO, OH, or CN in the IR spectra allow for the determination of the abundances of specific CNO isotopic species, such as  $^{12}\text{C}$ ,  $^{13}\text{C}$ ,  $^{14}\text{N}$ , and  $^{16}\text{O}$  here, or  $^{17}\text{O}$ ,  $^{18}\text{O}$ , and  $^{15}\text{N}$  in future studies.

The iron abundances sampled here range from  $[\text{Fe}/\text{H}] = -1.1$  to  $-0.3$ . Both  $[\text{Na}/\text{Fe}]$  and  $[\text{Ti}/\text{Fe}]$  are found to be consistently lower than their Galactic values by  $\sim -0.1$  to  $-0.5$  over the metallicity range sampled in the LMC. These characteristic underabundances of Na and Ti seem to also occur in a number of dwarf spheroidal galaxies (Shetrone et al. 2002).

The LMC red giants in this sample all show evidence of the mixing of CN-cycle material to their surfaces via the first dredge-up, with  $^{14}\text{N}$  enhanced by  $+0.4$  to  $+0.8$  dex over its estimated initial values, and  $^{12}\text{C}$  decreased by  $-0.3$  to  $-0.5$  dex. No evidence is found, in these predominantly first ascent giants or early AGB stars, of the extreme nitrogen enrichments ( $\sim +1.0$  dex or more) that might result from second dredge-up or hot bottom burning. The  $^{12}\text{C}/^{13}\text{C}$  ratios in the LMC red giants are found to decrease with decreasing giant star mass in a manner similar to that found for Galactic red giants (Gilroy 1989); however, the LMC trend appears to be shifted to lower  $^{12}\text{C}/^{13}\text{C}$  ratios for a given red-giant mass. This shift may be due to the increased mixing associated with lower-metallicity giants as suggested by Charbonnel et al. (1998).

A comparison of [O/Fe] versus [Fe/H] between the LMC and the Milky Way finds that the LMC trend falls below by about 0.2 dex over the range of [Fe/H]= -1.1 to -0.3. Good agreement in [O/Fe] as derived from a sample of F-supergiants (Hill et al. 1995), main-sequence B-stars (Korn et al. 2002), and the red giants analyzed here suggests that the difference between the LMC and the Milky Way is real. Lower values of [O/Fe] in the LMC can be explained by both a lower supernovae rate (caused by a lower star formation rate) and a lower ratio of supernovae type II to supernovae type Ia.

We thank the staff of Gemini South for their excellent assistance with these observations. Nick Suntzeff is to be thanked for insightful comments concerning the distance to the LMC. This work is supported in part by the National Science Foundation through AST99-87374 (V.V.S.).

## REFERENCES

Aaronson, M., & Mould, J. 1985, *ApJ*, 288, 551

Allende Prieto, C., Lambert, D. L., & Asplund, M. 2002, *ApJ*, 573, L137

Arnett, D. 1999, *Supernovae and Nucleosynthesis* (Princeton: Princeton University Press)

Asplund, M., Gustafsson, B., Kiselman, D., & Eriksson, K. 1997, *A&A*, 318, 521

Asplund, M., & Garcia Pérez, A. E. 2001, *A&A*, 372, 601

Balachandran, S. C. & Carney, B. W. 1996, *AJ* 111, 946

Barbuy, B. 1988, *A&A*, 191, 121

Barbuy, B., de Freitas Pacheco, J. A., & Castro, S. 1994, *A&A*, 283, 32

Bessell, M.S., & Brett, J.M. 1988, *PASP*, 100, 1134

Bessell, M.S., Castelli, F., & Plez, B. 1998, *A&A*, 333, 231

Bica, E., Geisler, D., Dottori, H., Clariá, J.J., Piatti, A.E., & Santos, J.F.C. Jr. 1998, *AJ*, 116, 723

Carpenter, J.M. 2001, *AJ*, 121, 2851

Charbonnel, C. 1994, *A&A*, 282, 811

Charbonnel, C., Brown, J. A., & Wallerstein, G. 1998, *A&A*, 332, 204

Cole, A. A., Smecker-Hane, T. A., & Gallagher, J. S., III 2000, *AJ*, 120, 1808

Costes, M., Naulin, C., & Dorthe, G. 1990, *A&A*, 232, 270

Cunha, K., Smith, V.V., & Lambert, D.L. 1995, *ApJ*, 452, 634

Da Costa, G. S. 1988 in *Harlow Shapley Symposium on Globular Cluster Systems in Galaxies*, edited by J. E. Grinlay and A. G. Davis Phillip (Reidel, Dordrecht), p. 191

D'Antona, F., & Mazzitelli, I. 1996, *ApJ*, 470, 1093

Dopita, M.A., Vassiliadis, E., Meatheringham, S.J., Bohlin, K;C;, Ford, H.C., Harrington, J.P., Wood, P.R., Stecher, T.P., & Maran, S.P. 1996, *ApJ*, 460, 320

Edvardsson, B., Andersen, J., Gustafsson, B., Lambert, D.L., Nissen, P.E. & Tomkin, J. 1993, *A&A*, 275, 101

Geisler, D., Bica, E., Dottori, H., Clariá, J.J., Piatti, A.E., & Santos, J.F.C. Jr. 1997, *AJ*, 114, 1920

Gilroy, K. K. 1989, *ApJ*, 347, 835

Goldman, A., Shoenfeld, W. G., Goorvitch, D., Chackerian C. Jr., Dothe, H., Mélen, F., Abrams, M. C. & Selby, J. E. A. 1998, *JQSRT*, 59, 45

Goorvitch, D. 1994, *ApJS*, 95, 535

Gratton, R.G., & Sneden, C. 1991, *A&A*, 241, 501

Grebel, E. K., Roberts, W. J. and Van de Rydt, F. 1994, Third ESO/CTIO Workshop, La Serena, Chile

Gustafsson, B., Bell, R. A., Eriksson, K., & Nordlund, A. 1975, *A&A*, 42, 407

Hill, V., Andrievsky, S., & Spite, M. 1995, *A&A*, 293, 347

Hill, V., Francois, P., Spite, M., Primas, F., & Spite, F. 2000, *A&A*, 364, L19

Hill, V., Plez, B., Cayrel, R., Beers, T. C., Nordstrom, B., Andersen, J., Spite, M., Spite, F., Barbuy, B., Bonifacio, P., Depagne, E., Francois, P., Primas, F. 2002, *A&A*, 387, 560

Hinkle, K. H., Wallace, L., & Livingston, W. 1995, Infrared Atlas of the Arcturus Spectrum, 0.9 - 5.3  $\mu$ m (San Francisco: Astronomical Society of the Pacific)

Hinkle, K. H., Cuberly, R., Gaughan, N., Heynssens, J., Joyce, R., Ridgway, S., Schmitt, P., & Simmons, J. E. 1998, *Proc. SPIE*, 3354, 810

Hinkle, K. H., Joyce, R. R., Sharp, N., & Valenti, J. A. 2000, *Proc. SPIE*, 4008, 720

Hinkle, K. H., Blum, R., Joyce, R. R., Ridgway, S. T., Rodgers, B., Sharp, N., Smith, V., Valenti, J., & van der Bliek, N. 2002, *Proc. SPIE*, 4834, in press

Holweger, H. 2001, in Solar and Galactic Composition (New York: American Institute of Physics), ed. R. F. Wimmer-Schweingruber, p.23

Huber, K. P. & Herzberg, G. 1979, Constants of Diatomic Molecules, Van Nostrand Reinhold, New York.

Iben, I., Jr. 1964, *ApJ*, 140, 1631

Keller, L. D., Pilachowski, C. A., & Sneden, C. 2001, *AJ*, 122, 2554

Korn, A. J., Becker, S. R., Gummersbach, C. A., & Wolf, B. 2000, *A&A*, 353, 655

Korn, A. J., Keller, S. C., Kaufer, A., Langer, N., Przybilla, N., Stahl, O., & Wolf, B. 2002, *A&A*, 385, 143

Kurucz, R.L., & Bell, B. 1995, CD-ROM 23

Luck, R. E., Moffett, T. J., Barnes, T. G., III, & Gieren, W. P. 1998, AJ, 115, 605

McWilliam, A. 1990, ApJS, 74, 1075

McWilliam, A. 1997 ARA&A 35, 503

Meléndez, J., Barbuy, B., & Spite, F. 2001, ApJ, 556, 858

Meléndez, J., & Barbuy, B. 2002, ApJ, 575, 474

Nissen, P.E., & Edvardsson, E. 1992, A&A, 261, 255

Nissen, P.E., Primas, F., Asplund, M., & Lambert, D.L. 2002, A&A, 390, 235

Olszewski, E.W., Schommer, R.A., Suntzeff, N.B., & Harris, H.C. 1991, AJ, 101, 515

Pagel, B. E. J. & Tautvaišienė, G. 1995, MNRAS, 276, 505

Plez, B., Brett, J.M., & Nordlund, Å. 1992, A&A, 256, 551

Prevot, L., Andersen, J., Ardeberg, A., Benz, W., Imbert, M., Lindgren, H., Martin, N., Maurice, E., Mayor, M., Nordstrom, B., Rebeiro, E., & Rousseau, J. 1985, A&AS, 62, 23

Russell, S. C., & Dopita, M. A. 1992, ApJ, 384, 508

Schaerer, D., Charbonnel, C., Meynet, G., Maeder, M., & Schaller, G. 1993, A&AS, 102, 339

Shetrone, M.D., Côté, P., & Sargent, W.L.W. 2001, ApJ, 548, 592

Smith, V.V., & Lambert, D.L. 1985, ApJ, 294, 326

Smith, V.V., & Lambert, D.L. 1986, ApJ, 311, 843

Smith, V.V., & Lambert, D.L. 1990, ApJS, 72, 387

Smith, V.V., Suntzeff, N.B., Cunha, K., Gallino, R., Busso, M., Lambert, D.L., & Straniero, O. 2000, AJ, 119, 1239

Smith, V.V., Cunha, K., & King, J. 2001, AJ, 122, 370

Sneden, C. 1973, ApJ, 184, 839

Spite, M., Hill, V., Primas, F., Francois, P., & Spite, F. 2001, New Astronomy Reviews, 45, 557

Fig. 1.— Sample spectra of the LMC red giant 2.3256 (K= 12.0) with each panel showing a different echelle grating tilt. Some of the stronger lines are identified. Each spectrum consists of a combination of three 1/2-hour integrations and the signal-to-noise in each spectrum is a bit more than 100 (see Table 2). These spectra are representative of the overall quality of the data analyzed here.

Fig. 2.— Modified Hertzsprung-Russell diagrams, with absolute bolometric magnitude versus effective temperature, for the red giants analyzed here, a few other LMC stellar samples with published abundances, and stellar model tracks from Schaefer et al. (1993). Note that previous LMC stellar abundance analyses tended to sample the more massive stars, while the red giants presented here have lower masses. The bottom panel shows an expanded view of the red giant region, with the model tracks terminated at the tip of the red giant branch. Models of AGB stars were computed by Karakas & Lattanzio (2002, private communication), however their tracks are complex and are not plotted here for clarity. The AGB tracks confirm that the red giants in this sample are either first ascent stars or early-AGB stars. Mass estimates for these LMC giants are based on the Schaefer et al. tracks and span a narrow range of  $\sim 2\text{-}4 M_{\odot}$ , except for the massive supergiant HV2586 and the lower-mass metal-poor giant NGC1898 AM6.

Fig. 3.— An illustration of the determination of the microturbulent velocity,  $\xi$ , for one red giant (AM1 in NGC2203). The left panels show the linear slopes resulting from fits to the carbon abundances (derived from CO lines) versus reduced equivalent width (top) and versus excitation potential (bottom) for various microturbulent velocities. No trend, i.e. zero slope, for both reduced equivalent width and excitation potential signifies a best fit. The effective temperature was set by IR colors, and note that a single value of  $\xi$  also results in a zero slope with excitation potential (which is most sensitive to  $T_{\text{eff}}$ ). The simultaneous solutions for both reduced equivalent width and excitation potential indicates a satisfactory fit for both  $T_{\text{eff}}$  and  $\xi$ . The right panels show the quality of the abundances for the given  $T_{\text{eff}}\text{-}\xi$  solution (a scatter of about  $\pm 0.06$  dex) for this star. The filled circles result from a model atmosphere extending to an optical depth at 5000Å of  $\tau = 10^{-4}$  (what we usually use as the upper atmospheric cut-off), while the open squares are the abundances resulting from truncating the atmosphere at  $\tau = 10^{-3}$ . As some of the  $^{12}\text{CO}$  lines are the strongest ones used, their insensitivity to model atmosphere details in the regime  $\tau = 10^{-3}$  to  $10^{-4}$  indicates that the atmospheric structure is adequate for this abundance analysis.

Fig. 4.— Microturbulent velocities, as determined for Galactic M-giants (open circles), or MS- and S-stars (open triangles) from Smith & Lambert (1985; 1986; 1990), and the LMC red giants (filled circles) versus absolute bolometric magnitude (top panel) and logarithm of the surface gravity (bottom panel). The overlap in  $\xi$  with both  $M_{\text{bol}}$  and  $\log g$  between the Galactic giants and the LMC giants is excellent. At lower luminosity (with  $M_{\text{bol}} \geq -3$ ) and larger  $\log g$  ( $\geq 1$ ), there is an almost constant microturbulence of  $\xi \sim 2.0\text{-}2.5 \text{ km s}^{-1}$ . As luminosity increases and surface gravity decreases,  $\xi$  increases slowly towards  $3.0\text{-}3.5 \text{ km s}^{-1}$ , with the Galactic and LMC giants following a similar trend.

Fig. 5.— Sample synthetic and real spectra in two spectral regions in two different stars. The top panel illustrates a small spectral region in the K-band showing three  $^{12}\text{CO}$  lines, of differing strengths, and an atomic Sc I line. The open circles are the observed data, while the continuous curves are synthetic spectra with differing carbon and scandium abundances (as shown on the figure). Note that the three  $^{12}\text{CO}$  lines, with very different equivalent widths and excitation potentials, yield nearly the same  $^{12}\text{C}$  abundance. The bottom panel shows two OH lines in the H-band, again with the open circles being the real spectrum and the continuous curves showing synthetic spectra with differing  $^{16}\text{O}$  abundances.

Fig. 6.— Examples of synthetic spectral fits to the blended  $^{13}\text{CO}$  (2-0) bandhead in two LMC red giants. The top panel shows a field star (2.1158) that has an estimated mass of  $3\text{M}_\odot$ , with a metallicity of  $[\text{Fe}/\text{H}] = -0.34$ , and having a fairly large  $^{12}\text{C}/^{13}\text{C}$  ratio, typical of the slightly higher mass red giants in this sample. The bottom panel illustrates the  $^{13}\text{CO}$  bandhead in the most metal-poor star in the sample, the cluster member AM6 in NGC1898, with  $[\text{Fe}/\text{H}] = -1.13$ . This is an old LMC red giant, with an estimated mass of  $1\text{M}_\odot$ , and having a low isotopic ratio ( $^{12}\text{C}/^{13}\text{C} = 3.5$ ); the trend in the LMC of lower carbon isotope ratios with lower mass and metallicity is in the same sense as in the Milky Way.

Fig. 7.— A comparison of field star iron abundances from the large study by Cole et al. (2000- top panel) and for the field LMC red giants analyzed here. The Cole et al. results are derived from low-resolution spectra of the Ca II IR triplet, while  $[\text{Fe}/\text{H}]$  for the stars here are from three Fe I lines in the H-band. Our current sample of 9 field stars is too small to compare to the shape of the metallicity distribution as defined by the Cole et al. (2000) sample; however, the average  $[\text{Fe}/\text{H}]$  of our sample agrees very well with that expected from the Cole et al. distribution.

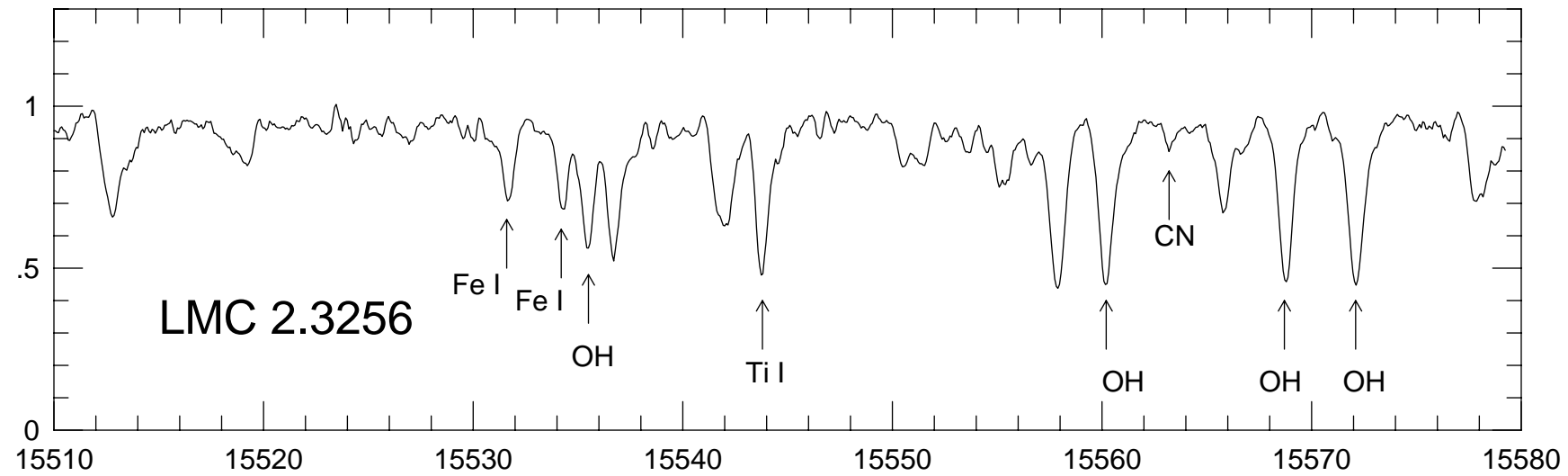
Fig. 8.— Abundances of  $^{14}\text{N}$  versus  $^{12}\text{C}$  (on the scale of  $A(x) = \log[\text{N}(x)/\text{N}(\text{H})] + 12$ ) for the LMC red giants along with other LMC samples, as well as Galactic red giants (from Smith & Lambert 1985; 1986; 1990). The solid curves illustrate “CN mixing lines”: since the CN cycle, operating by itself, will conserve the total C plus N nuclei, the curves represent these relations. No account is taken of some carbon cycled into  $^{13}\text{C}$ , however in the extreme case of the steady state CN-cycle, this would shift the  $^{12}\text{C}$  abundances by, at most, 0.1 dex towards lower values. In the case of the Galactic M-giants, they are approximated reasonably well by CN-cycle mixing in near-solar metallicity material. Some of the very  $^{14}\text{N}$ -rich MS or S stars have converted some  $^{16}\text{O}$ , or  $^{12}\text{C}$  produced during  $^4\text{He}$ -burning, into nitrogen. The LMC red giants fall along CN mixing lines that are defined well by initial carbon and nitrogen abundances as derived by Korn et al. (2002) for main-sequence B-stars in the young LMC cluster NGC2004.

Fig. 9.— Carbon-12 to carbon-13 ratios versus stellar mass in the LMC red giants and in Galactic open-cluster giants from Gilroy (1989). The LMC masses are estimated from the evolutionary tracks of Schaerer et al. (1993). The trend of a lower  $^{12}\text{C}/^{13}\text{C}$  ratio with a lower stellar mass observed in the LMC sample of giants is in qualitative agreement with the result found by Gilroy (1989) for the Galactic giants. The noticeable offset between LMC and Galactic trends may be due

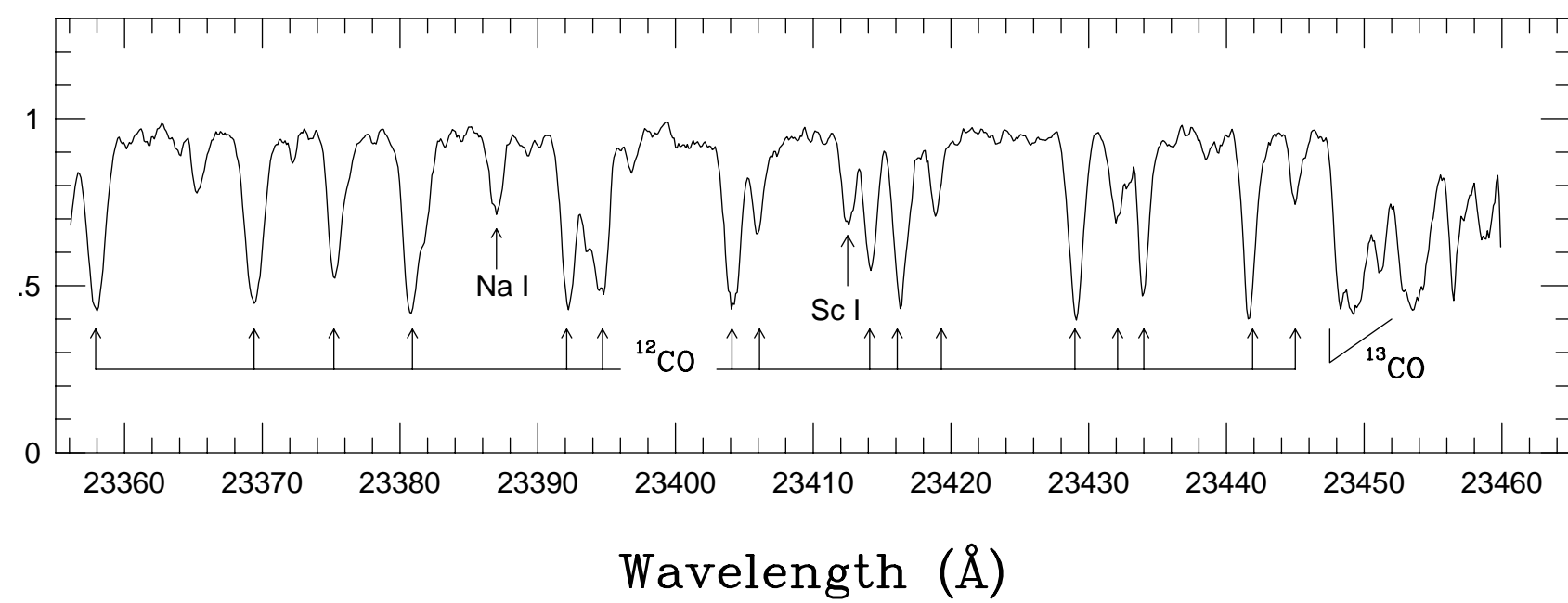
to an increase in extra-mixing efficiency on the giant branch with decreasing metallicity as argued by Charbonnel et al. (1998).

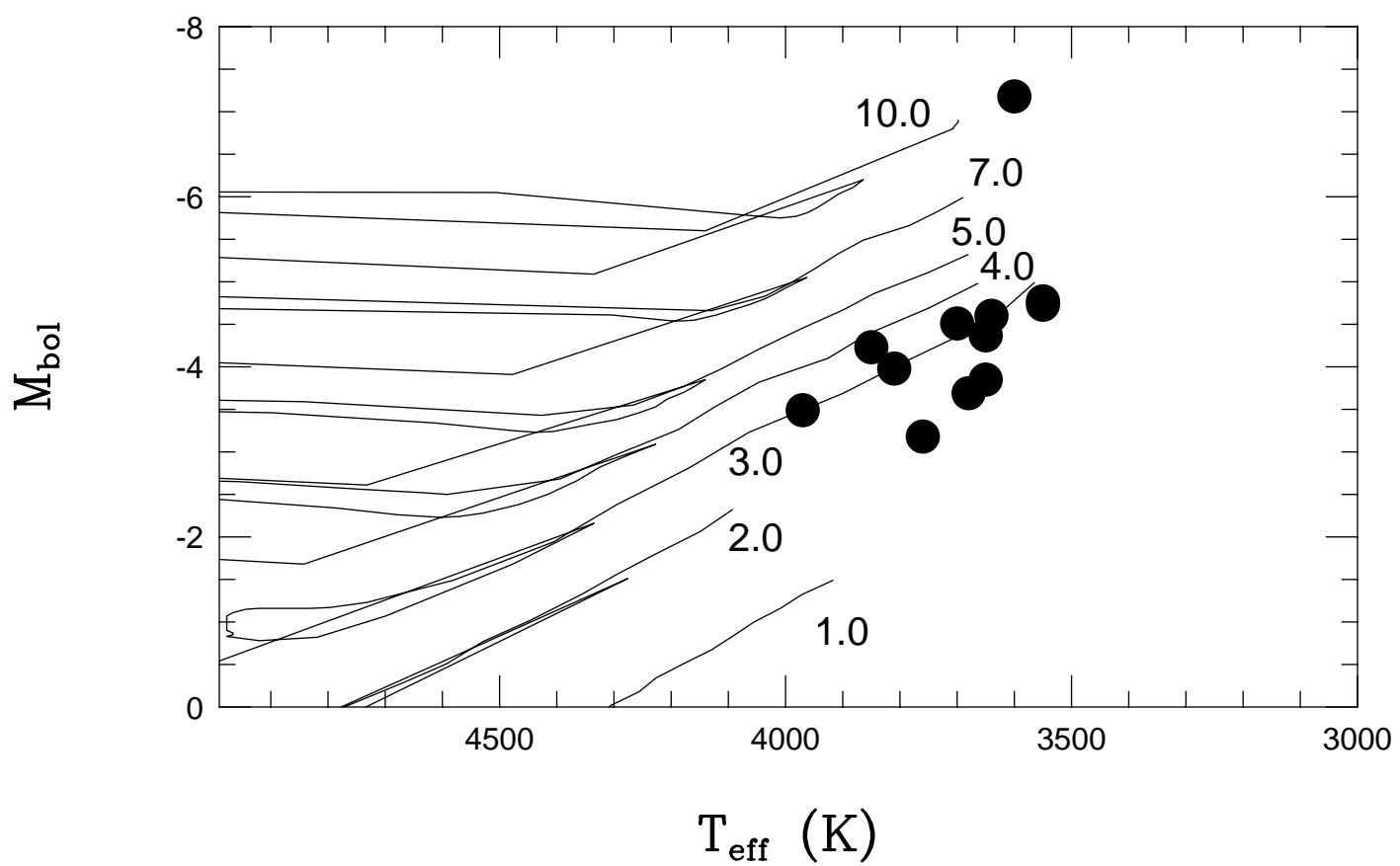
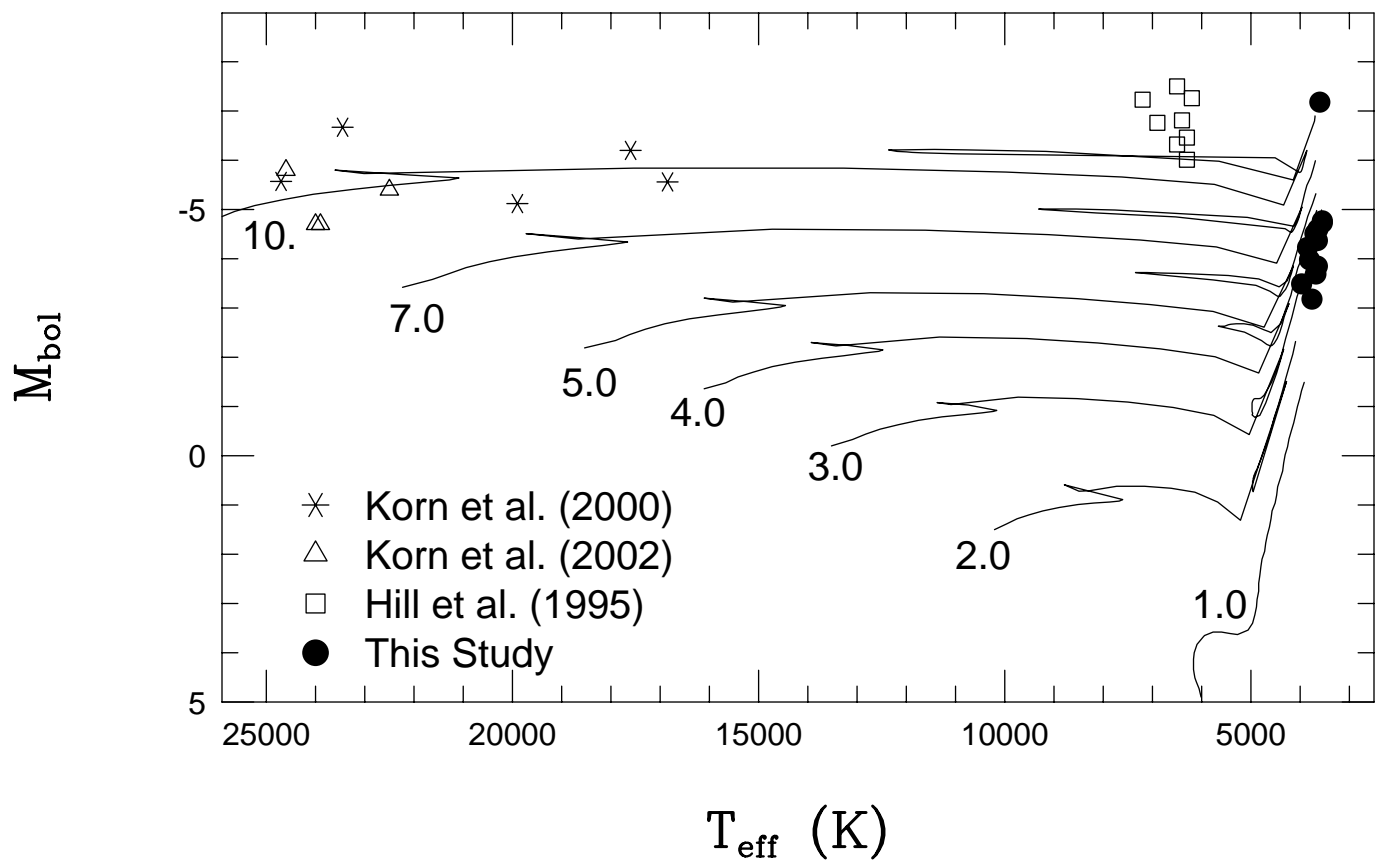
Fig. 10.— Values of [O/Fe] versus [Fe/H] for the LMC red giants, along with other samples of LMC and Galactic stars. Most of the Galactic results rely on the [O I] line near 6300Å, weak O I lines near 6158Å, or IR vibration-rotation OH lines (as used here). The LMC F-supergiants from Hill et al. (1995) rely on the weak O I lines near 6158Å, while the Korn et al. (2002) results for the hot B-stars use lines of O II and Fe III. All three samples of LMC stars indicate a trend of [O/Fe] that falls  $\sim 0.2$  dex below the Galactic trend at  $[\text{Fe}/\text{H}] \sim -0.5$  to 0.0. The fact that three quite different samples of stars provide such a consistent result is a strong indication that [O/Fe] is low in the LMC compared to the Milky Way at near-solar values of [Fe/H]. The continuous curves are simple models of chemical evolution in which supernovae of type II and Ia add O and Fe into mixed gas. The LMC curve differs from the Milky Way curve by having a SN II rate that is 3 times lower and a SN Ia rate that is 2 times lower.

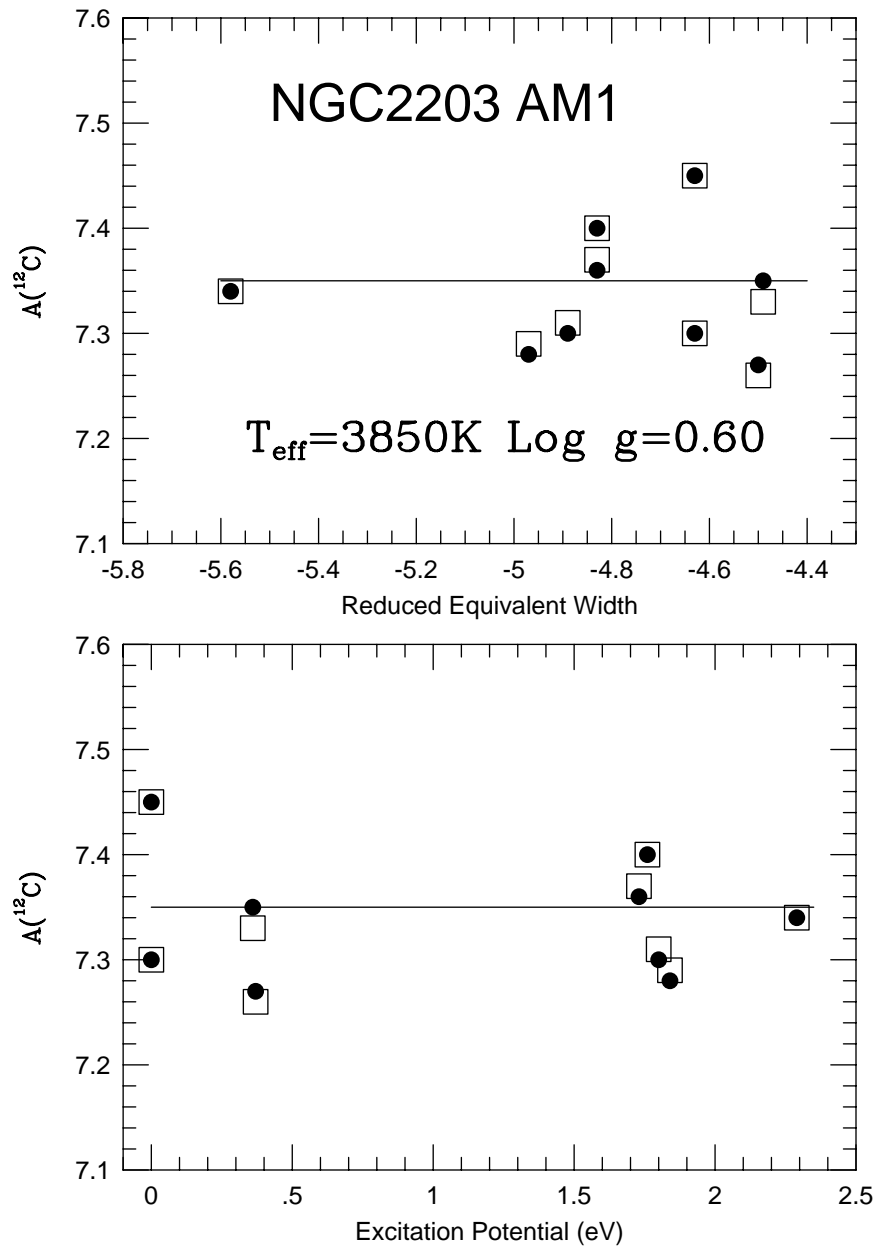
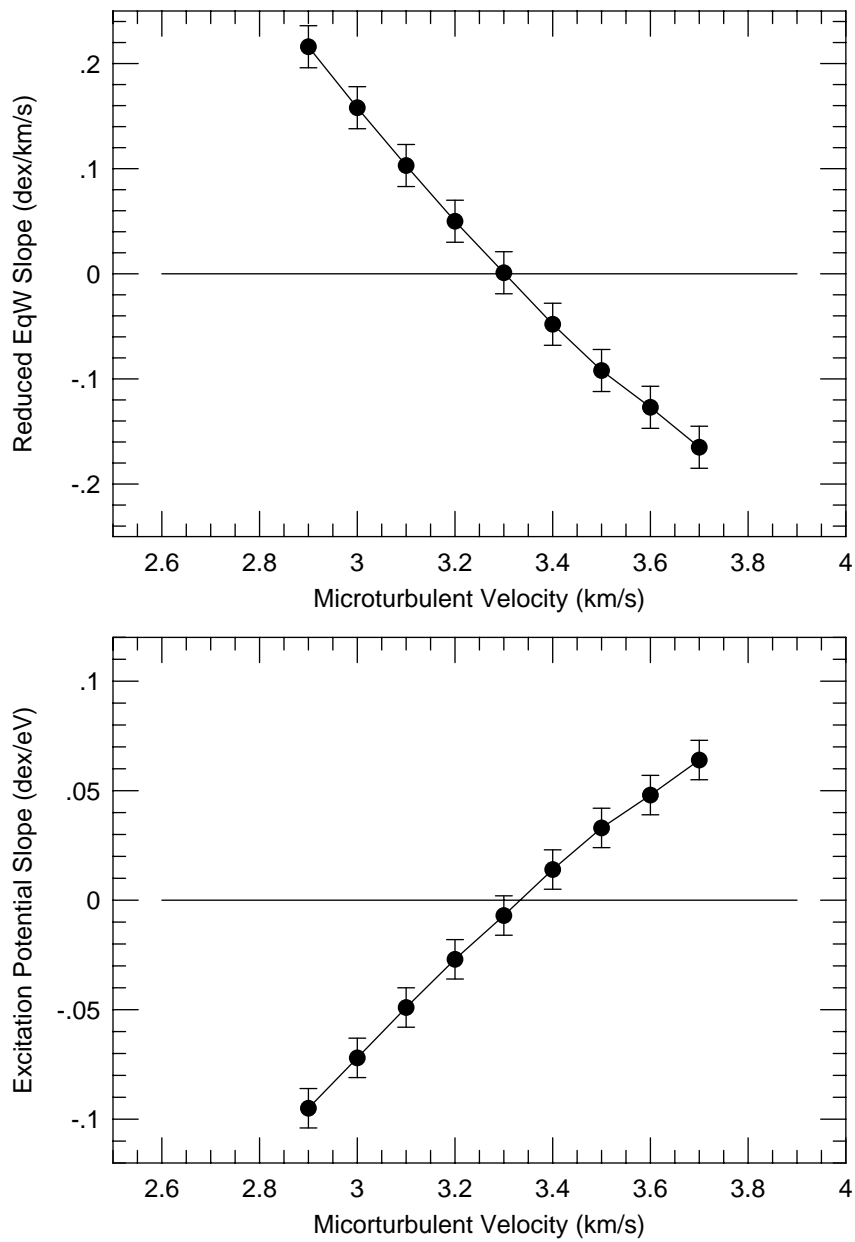
Relative Flux

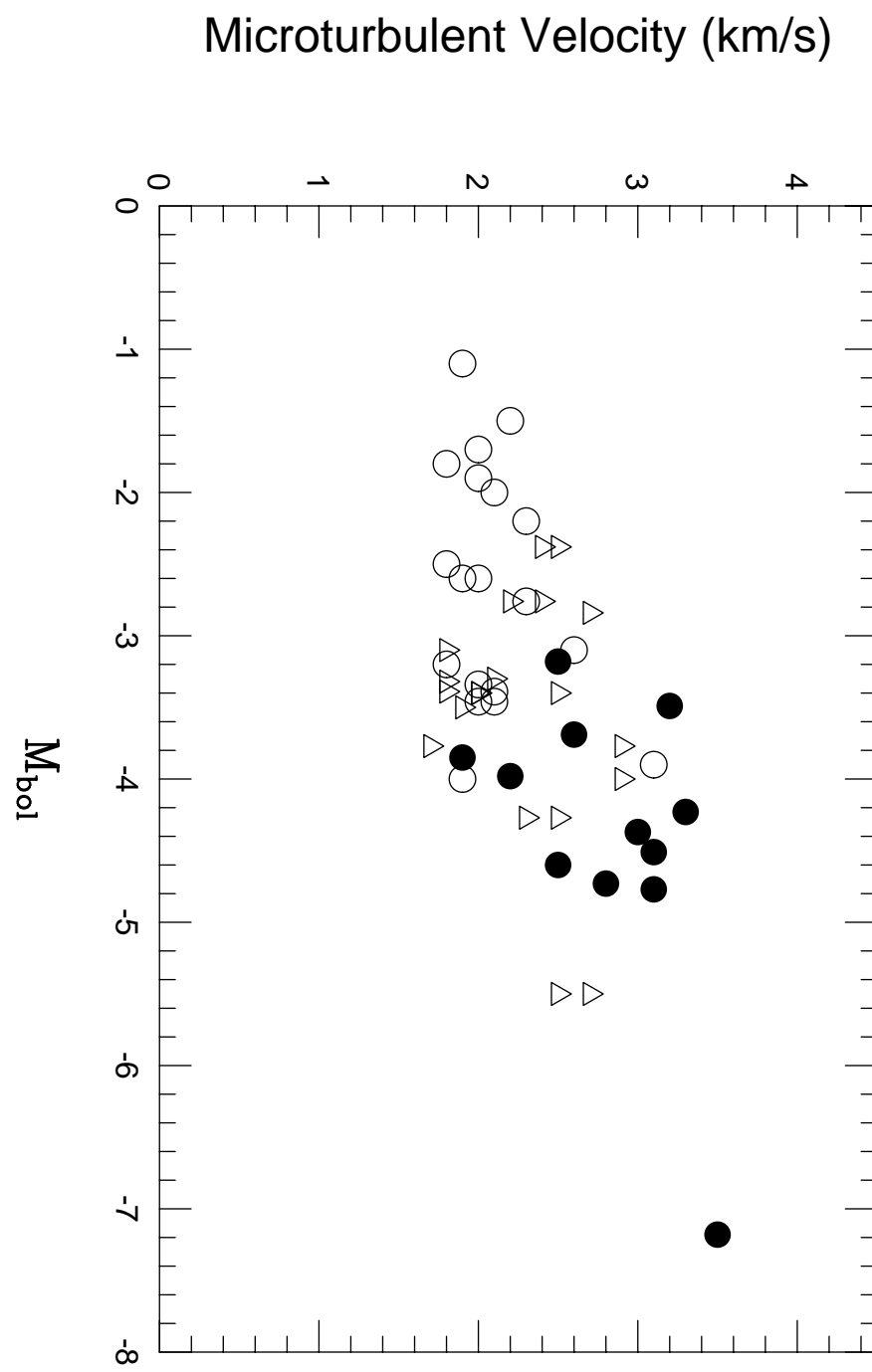
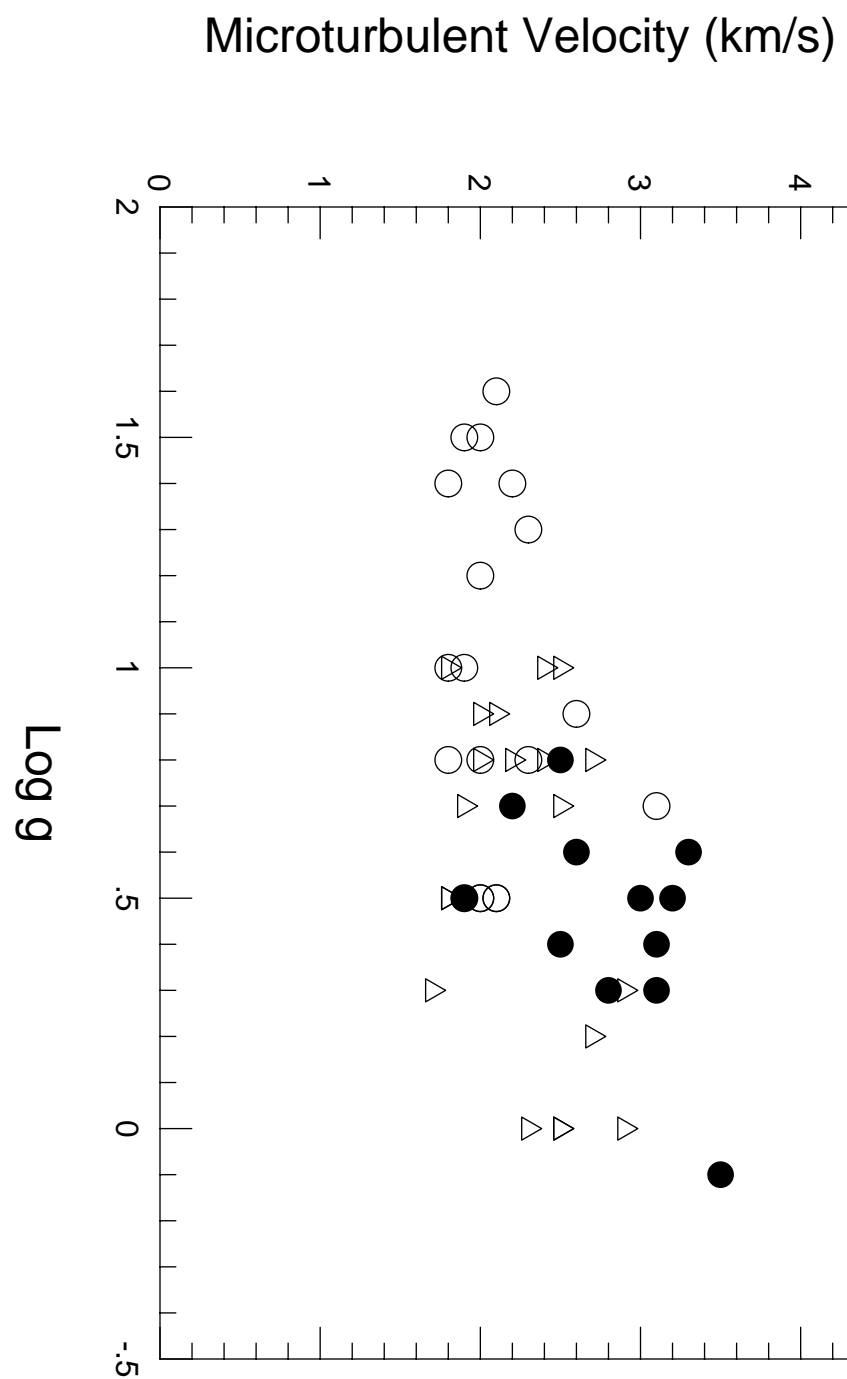


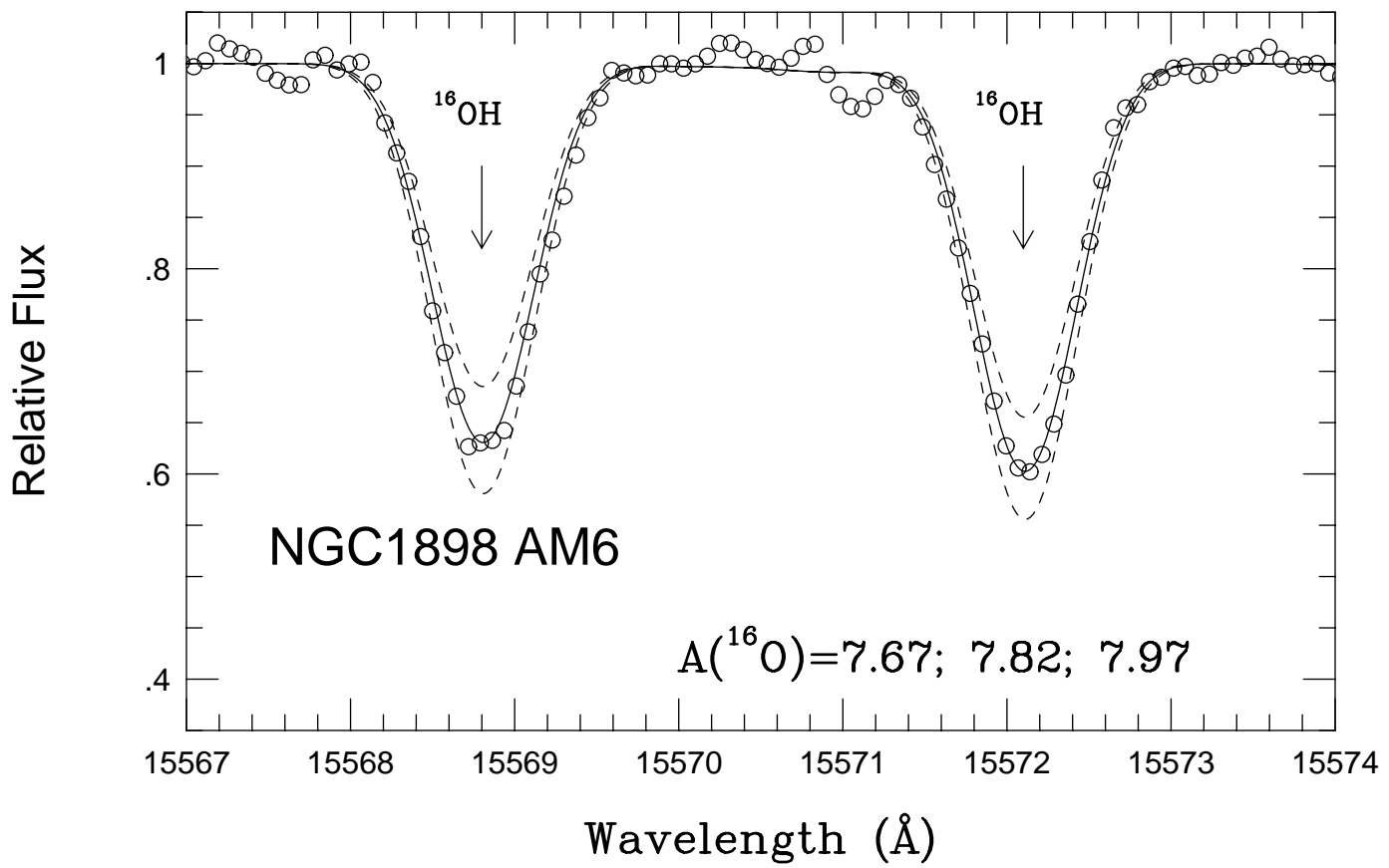
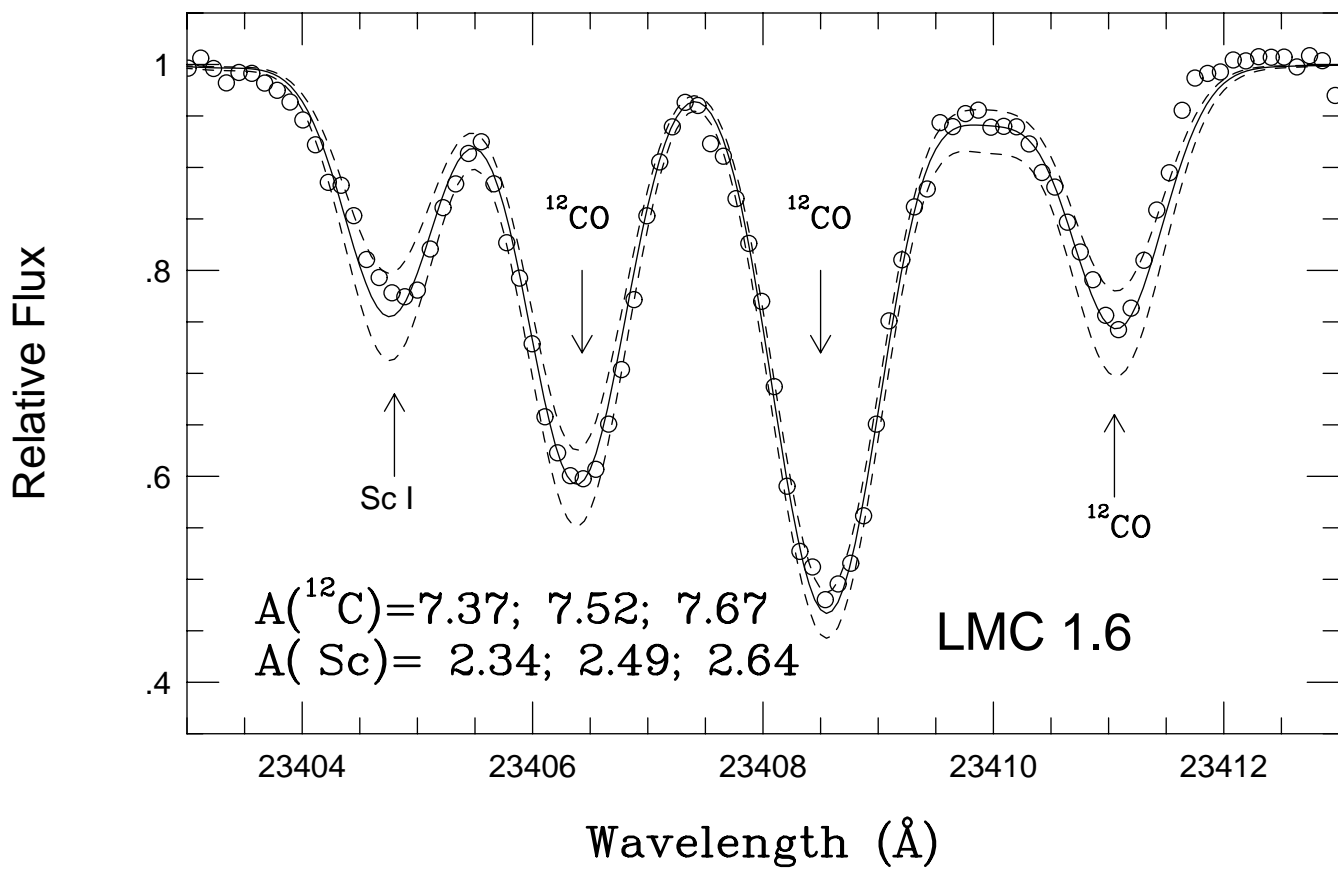
Relative Flux

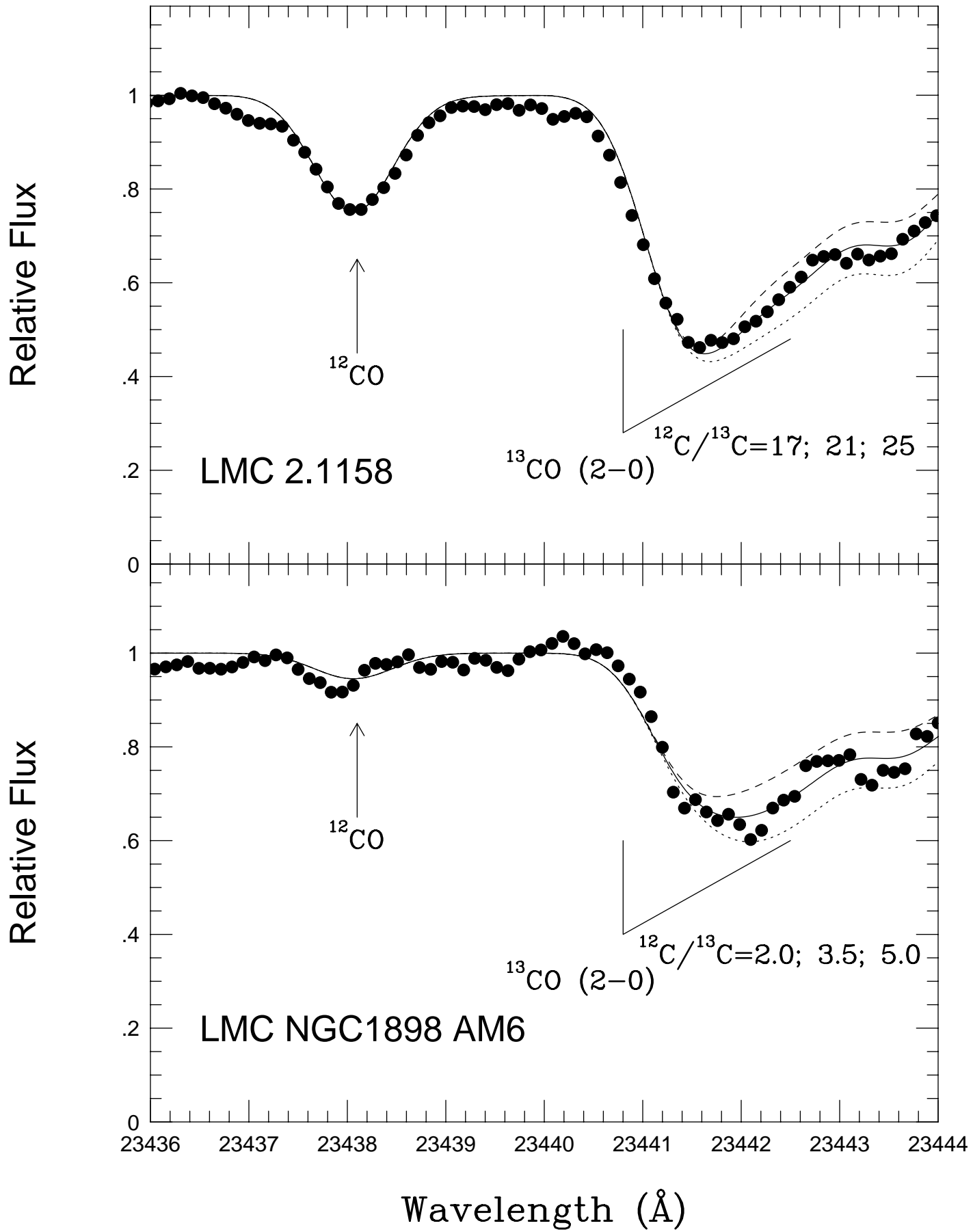


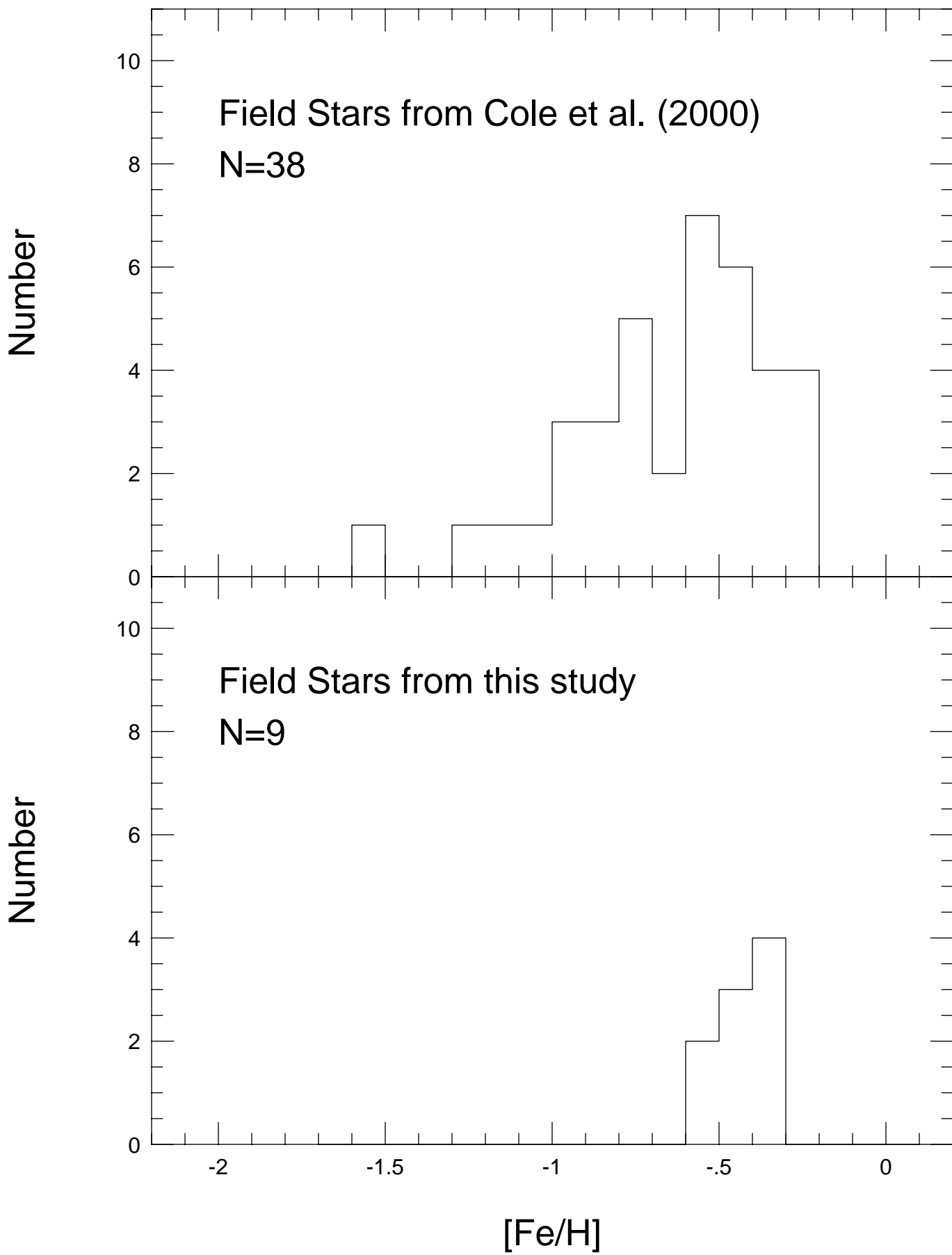


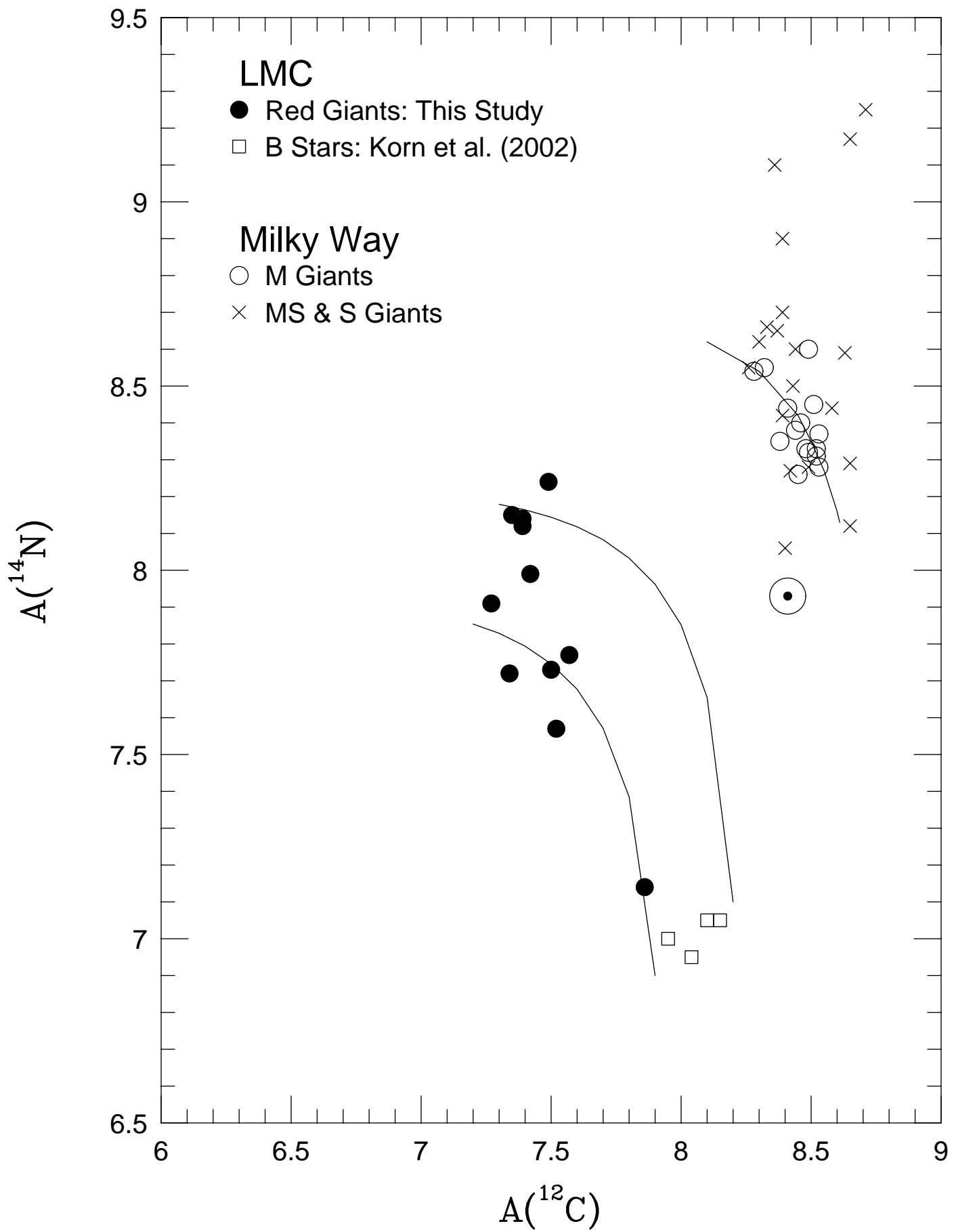


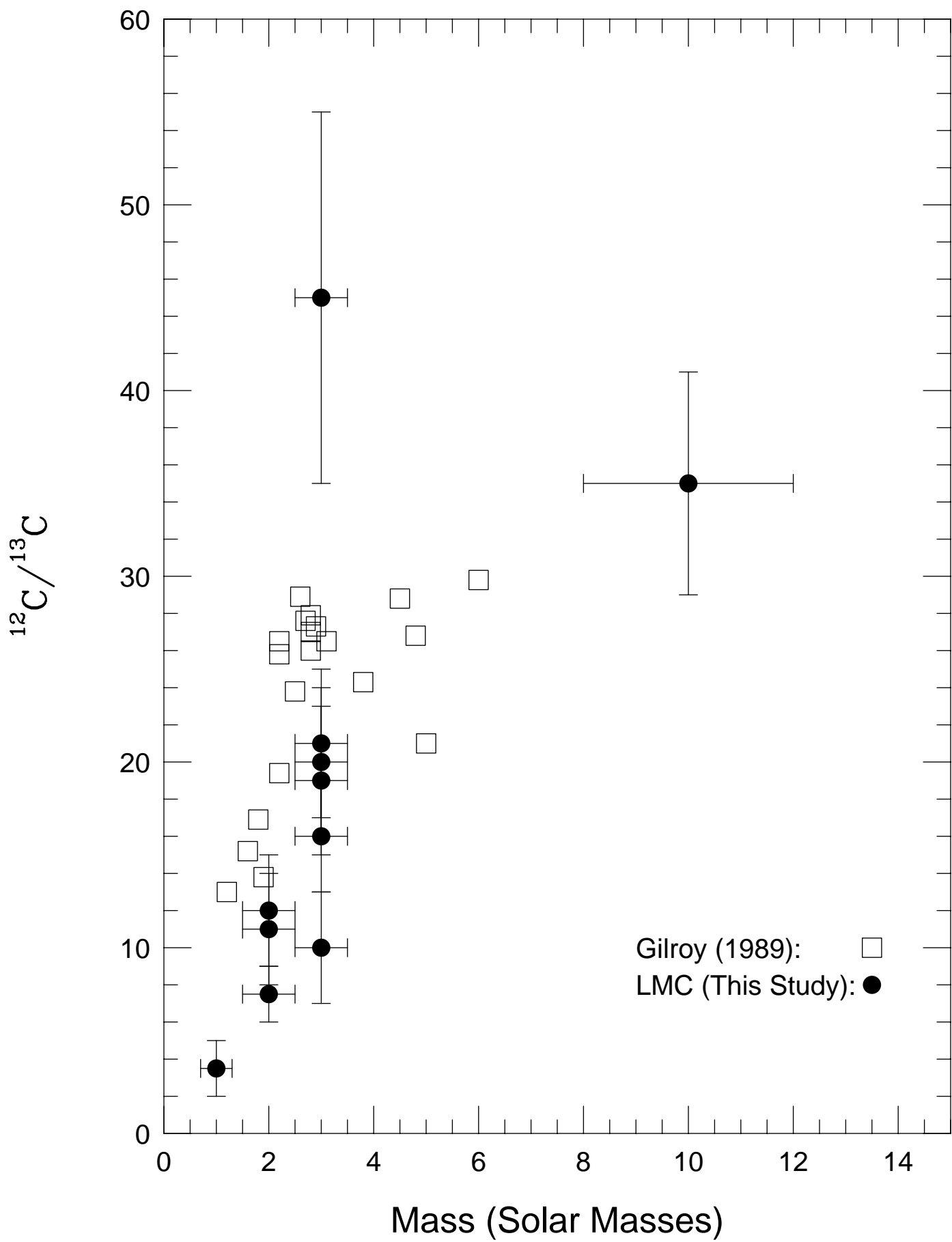












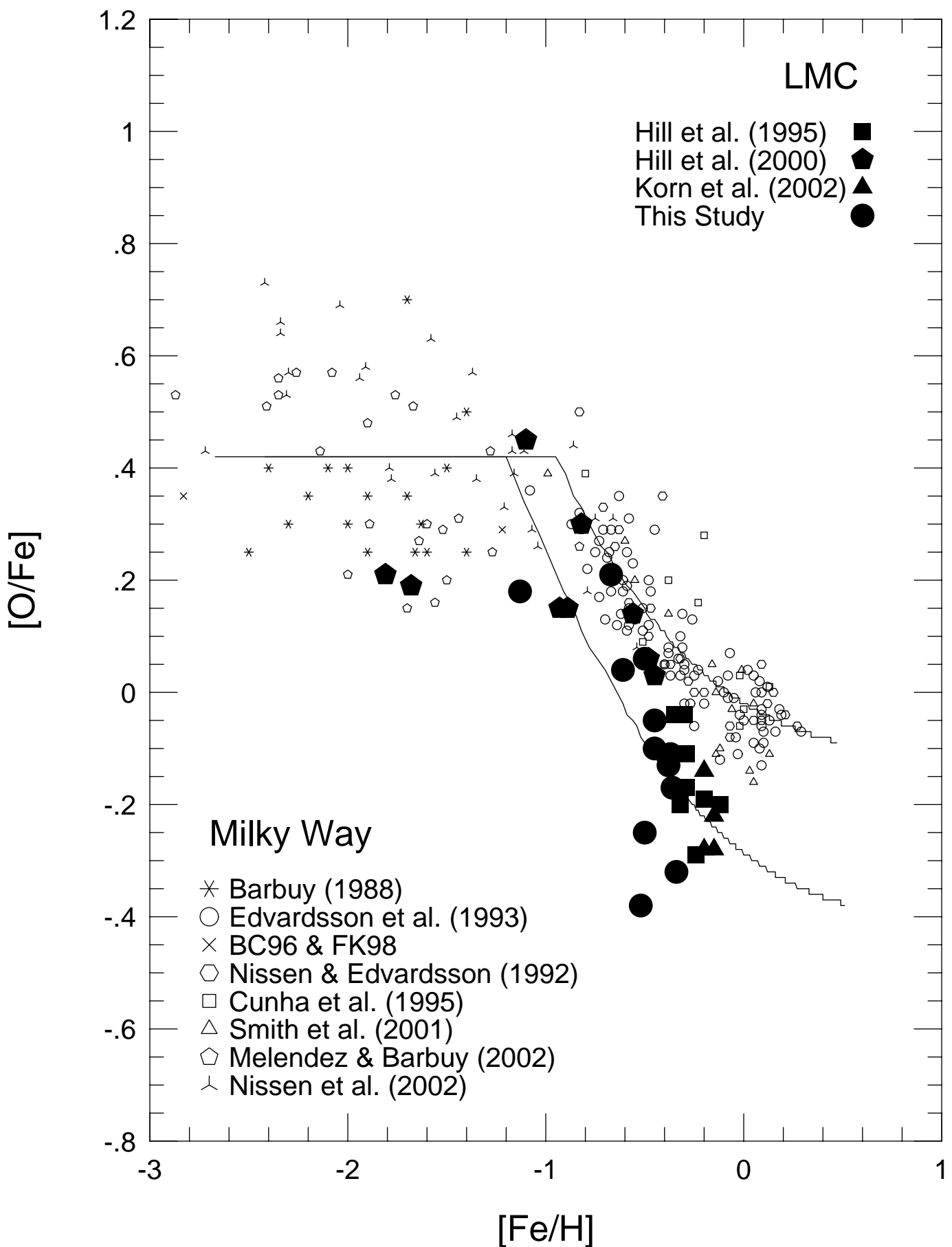


Table 1. Program Stars

Star	K	(J-K)	RA (J2000)	DEC (J2000)
1.6	12.60	1.08	05 23 18.93	-69 45 45.5
1.27	10.80	1.26	05 24 00.84	-69 45 44.0
1.50	10.84	1.26	05 23 28.56	-69 48 26.1
2.1158	11.08	1.16	05 31 19.77	-69 58 29.5
2.3256	12.03	1.13	05 32 41.54	-69 53 33.3
2.4525	11.32	1.15	05 31 31.49	-70 04 15.6
2.5368	11.84	1.15	05 30 34.81	-70 02 33.9
HV 2568	8.48	1.18	05 29 34.41	-66 55 28.4
NGC1898 AM5	11.82	1.06	05 16 38.80	-69 39 35.3
NGC1898 AM6	12.42	0.98	05 16 44.80	-69 39 28.3
NGC2203 AM1	11.32	1.05	06 04 47.68	-75 25 43.7
NGC2203 AM2	11.21	1.12	06 04 47.57	-75 25 42.9

Table 2. Observations Log

Star		$\lambda 15540\text{\AA}$	$(S/N)_{15540}$	$\lambda 23400\text{\AA}$	$(S/N)_{23400}$
1.6	21 Dec. 2001: 3x1200s	65	04 Feb. 2002: 4x1800s	95	
1.27	21 Dec. 2001: 2x1800s	155	02 Feb. 2002: 3x600s	105	
1.50	05 Feb. 2002: 4x600s	150	02 Feb. 2002: 3x600s	120	
2.1158	05 Feb. 2002: 3x1200s	200	03 Feb. 2002: 3x1200s	225	
2.3256	07 Feb. 2002: 3x1800s	105	03 Feb. 2002: 3x1800s	115	
2.4525	05 Feb. 2002: 3x900s	90	04 Feb. 2002: 3x1200s	100	
2.5368	05 Feb. 2002: 3x1800s	75	03 Feb. 2002: 3x1800s	125	
HV 2586	21 Dec. 2001: 2x600s	210	23 Dec. 2001: 4x600s	220	
NGC1898 AM5	06 Feb. 2002: 3x1800s	70	09 Feb. 2002: 3x1200s	105	
NGC1898 AM6	06 Feb. 2002: 3x1800s	50	09 Feb. 2002: 3x1800s	95	
NGC2203 AM1	21 Dec. 2001: 4x1200s	125	02 Feb. 2002: 3x1200s	115	
NGC2203 AM2	21 Dec. 2001: 4x1200s	80	02 Feb. 2002: 3x1200s	80	

Table 3. Derived Stellar Parameters

Star	$M_{\text{bol}}$	$T_{\text{eff}}$ (K)	Mass ( $M_{\odot}$ )	$\log g$ ( $\text{cm s}^{-2}$ )	$\xi$ ( $\text{km s}^{-1}$ )	[Fe/H]	$V_r$ ( $\text{km s}^{-1}$ )
1.6	-3.18	3760	2	+0.8	2.5	-0.50	+262.0±0.3
1.27	-4.77	3550	3	+0.3	3.1	-0.36	+246.0±0.5
1.50	-4.73	3550	3	+0.3	2.8	-0.37	+263.9±0.8
2.1158	-4.60	3640	3	+0.4	2.5	-0.34	+281.6±0.5
2.3256	-3.69	3680	2	+0.6	2.6	-0.45	+229.8±0.4
2.4525	-4.37	3650	3	+0.5	3.0	-0.45	+251.4±0.4
2.5368	-3.85	3650	2	+0.5	1.9	-0.38	+232.2±0.5
HV 2586	-7.18	3600	10	-0.1	3.5	-0.52	+289.6±1.2
NGC1898 AM5	-3.98	3810	3	+0.7	2.2	-0.50	+254.7±0.4
NGC1898 AM6	-3.49	3970	1	+0.5	3.2	-1.13	+219.3±0.3
NGC2203 AM1	-4.23	3850	3	+0.6	3.3	-0.67	+253.4±0.6
NGC2203 AM2	-4.51	3700	3	+0.4	3.1	-0.61	+253.1±0.8

Table 4. Spectral-Line Data &amp; Equivalent Widths.

$\lambda(\text{\AA})$	$\chi(\text{eV})$	log gf	01	02	03	04	05	06	07	08	09	10	11	12
Fe I														
15531.742	5.64	-0.564	141	182	171	189	169	178	146	214	175	—	170	198
15534.239	5.64	-0.402	253	275	253	290	174	211	208	230	176	128	244	195
15537.572	5.79	-0.799	106	169	105	142	83	136	79	125	58	41	116	90
Na I														
23378.945	3.75	-0.420	376	418	427	476	277	402	398	294	322	95	364	442
Sc I														
23404.756	1.44	-1.278	213	617	496	327	321	472	354	602	240	74	476	668
Ti I														
15543.720	1.88	-1.481	382	482	427	428	327	442	353	415	345	188	532	452
$^{12}\text{C}^{14}\text{N}$														
15530.987	0.89	-1.519	108	163	197	150	47	—	—	—	48	—	120	126
15544.501	1.15	-1.146	67	142	111	84	81	87	65	181	47	—	99	78
15552.747	0.90	-1.680	—	127	112	85	48	23	38	—	20	25	78	—
15553.659	1.08	-1.285	30	143	123	115	72	81	78	160	37	—	97	93
15563.376	1.15	-1.141	85	130	140	122	46	68	78	182	64	—	95	102
$^{12}\text{C}^{16}\text{O}$														
23396.305	0.37	-5.167	611	869	933	781	736	741	555	1033	543	485	732	837
23398.275	1.73	-4.438	310	391	390	359	308	334	316	420	374	96	349	431
23406.389	0.00	-6.565	482	648	794	531	444	535	526	612	436	312	573	635
23408.555	0.36	-5.190	640	771	855	657	668	772	620	1119	604	426	755	866
23411.070	1.76	-4.430	212	419	442	344	321	282	293	580	406	80	348	334
23424.328	1.80	-4.427	255	287	262	273	303	279	280	329	183	92	304	211
23426.322	0.00	-6.744	418	511	549	461	482	528	398	—	615	177	550	541
23431.240	2.29	-4.757	77	136	110	80	61	85	95	—	120	56	62	50
23438.059	1.84	-4.414	214	299	309	230	162	261	230	300	315	39	250	181
$^{16}\text{OH}$														
15535.489	0.51	-5.233	277	398	392	277	300	340	261	327	213	228	388	326
15560.271	0.30	-5.307	246	527	525	415	392	491	374	366	367	286	518	421
15568.807	0.30	-5.270	243	517	470	340	396	463	372	372	312	315	500	405
15572.111	0.30	-5.270	291	505	466	363	442	463	384	387	313	295	477	398

Note. — Star Column ID: 01=1.6, 02=1.27, 03=1.50, 04=2.1158, 05=2.3256, 06=2.4525, 07=2.5368, 08=HV2586, 09=NGC1898 AM5, 10=NGC1898 AM6, 11=NGC2203 AM1, 12=NGC2203 AM2.

Table 5. Sensitivity of Abundances to Stellar Parameters

Element	$\Delta T_{\text{eff}} = +100\text{K}$	$\Delta \log g = +0.2$	$\Delta \xi = +0.2 \text{ km s}^{-1}$	$\Delta_{\text{tot}}$
$\Delta \text{Fe}$	-0.10	+0.05	-0.04	0.12
$\Delta \text{C}$	+0.05	-0.15	-0.06	0.17
$\Delta \text{N}$	-0.11	+0.18	-0.01	0.21
$\Delta \text{O}$	+0.22	+0.01	-0.09	0.24
$\Delta \text{Na}$	+0.09	-0.04	-0.04	0.11
$\Delta \text{Sc}$	+0.19	-0.02	-0.06	0.20
$\Delta \text{Ti}$	+0.16	+0.00	-0.08	0.18

Table 6. Abundances

Star	A(Fe)	A( $^{12}\text{C}$ )	$^{12}\text{C}/^{13}\text{C}$	A( $^{14}\text{N}$ )	A( $^{16}\text{O}$ )	A(Na)	A(Sc)	A(Ti)
1.6	7.00 $\pm$ 0.10	7.52 $\pm$ 0.11	11 $\pm$ 3	7.57 $\pm$ 0.15	8.02 $\pm$ 0.17	5.65	2.49	4.55
1.27	7.14 $\pm$ 0.13	7.39 $\pm$ 0.16	...	8.14 $\pm$ 0.09	8.24 $\pm$ 0.11	5.60	2.80	4.31
1.50	7.13 $\pm$ 0.05	7.49 $\pm$ 0.08	16 $\pm$ 3	8.24 $\pm$ 0.11	8.29 $\pm$ 0.15	5.55	2.72	4.39
2.1158	7.16 $\pm$ 0.06	7.38 $\pm$ 0.14	21 $\pm$ 4	8.12 $\pm$ 0.16	8.11 $\pm$ 0.15	5.68	2.61	4.44
2.3256	7.05 $\pm$ 0.09	7.50 $\pm$ 0.10	12 $\pm$ 3	7.73 $\pm$ 0.16	8.22 $\pm$ 0.09	5.34	2.61	4.15
2.4525	7.05 $\pm$ 0.10	7.34 $\pm$ 0.13	10 $\pm$ 3	7.72 $\pm$ 0.18	8.29 $\pm$ 0.13	5.38	2.80	4.24
2.5368	7.12 $\pm$ 0.10	7.57 $\pm$ 0.10	7.5 $\pm$ 1.5	7.77 $\pm$ 0.13	8.26 $\pm$ 0.15	5.80	2.65	4.61
HV 2586	6.98 $\pm$ 0.09	7.27 $\pm$ 0.13	35 $\pm$ 6	7.91 $\pm$ 0.05	7.87 $\pm$ 0.15	5.84	2.50	4.19
NGC1898 AM5	7.00 $\pm$ 0.12	7.86 $\pm$ 0.15	20 $\pm$ 4	7.14 $\pm$ 0.15	8.33 $\pm$ 0.16	5.71	2.60	4.54
NGC1898 AM6	6.37 $\pm$ 0.05	6.53 $\pm$ 0.09	3.5 $\pm$ 1.5	...	7.82 $\pm$ 0.08	4.69	2.01	3.84
NGC2203 AM1	6.83 $\pm$ 0.11	7.35 $\pm$ 0.08	19 $\pm$ 4	8.15 $\pm$ 0.13	8.31 $\pm$ 0.13	5.25	2.85	4.27
NGC2203 AM2	6.89 $\pm$ 0.07	7.42 $\pm$ 0.06	45 $\pm$ 10	7.99 $\pm$ 0.08	8.20 $\pm$ 0.14	5.57	2.91	4.30
Sun	7.50	8.59	89	8.00	8.77	6.33	3.17	5.02
$\alpha$ Boo	6.78	7.79 $\pm$ 0.08	8.0 $\pm$ 1.0	7.65 $\pm$ 0.07	8.39 $\pm$ 0.05	5.85	2.64	4.64

Note. — A(x)=  $\log[\text{N}(x)/\text{N}(\text{H})] + 12$ .